THEORETICAL ANALYSIS OF SMALL CRACK GROWTH IN FIBER-REINFORCED CERAMIC COMPOSITE MATERIALS

by

FORREST T PATTERSON

B.S., Mechanical Engineering
University of California, Berkeley (1989)

M.S., Mechanical Engineering
Stanford University (1990)

Submitted to the Department of
Mechanical Engineering
in Partial Fulfillment of the Requirements
for the Degree of

DOCTOR OF PHILOSOPHY
IN MECHANICAL ENGINEERING
at the
MASSACHUSETTS INSTITUTE OF TECHNOLOGY
May 1994

Signature of Author F.T. Patterson
Department of Mechanical Engineering
May, 1994

Certified by
Professor Michael P. Cleary
Thesis Supervisor

Accepted by
Professor Ain A. Sonin
Chairman, Mechanical Engineering Department Committee

REPORT DOCUMENTATION PAGE

AFRL-SR-BL-TR-98-

0370

1. AGENCY USE ONLY (Leave Blank)	2. REPORT DATE	3. REPORT
	May 1994	Final

4. TITLE AND SUBTITLE
Theoretical Analysis of Small Crack Growth in Fiber-Reinforced Ceramic Composite Materials

5. FUNDING NUMBERS

6. AUTHORS
Forrest T. Patterson

7. PERFORMING ORGANIZATION NAME(S) AND ADDRESS(ES)
Massachusetts Institute of Technology

8. PERFORMING ORGANIZATION REPORT NUMBER

9. SPONSORING/MONITORING AGENCY NAME(S) AND ADDRESS(ES)
AFOSR/NI
110 Duncan Avenue, Room B-115
Bolling Air Force Base, DC 20332-8080

10. SPONSORING/MONITORING AGENCY REPORT NUMBER

11. SUPPLEMENTARY NOTES

12a. DISTRIBUTION AVAILABILITY STATEMENT
Approved for Public Release

12b. DISTRIBUTION CODE

13. ABSTRACT *(Maximum 200 words)*
See attached.

14. SUBJECT TERMS

15. NUMBER OF PAGES

16. PRICE CODE

17. SECURITY CLASSIFICATION OF REPORT	18. SECURITY CLASSIFICATION OF THIS PAGE	19. SECURITY CLASSIFICATION OF ABSTRACT	20. LIMITATION OF ABSTRACT
Unclassified	Unclassified	Unclassified	UL

THEORETICAL ANALYSIS OF SMALL CRACK GROWTH IN FIBER-REINFORCED CERAMIC COMPOSITE MATERIALS

by

FORREST T PATTERSON

Submitted to the Department of Mechanical Engineering
in May, 1994 in partial fulfillment of the
requirements for the Degree of Doctor of Philosophy

Abstract

This research program investigates matrix crack initiation and subsequent propagation in fiber-reinforced ceramic materials for use in high-temperature structural applications.

Though it presents a formidable manufacturing challenge, the inclusion of ceramic fibers promises to increase fracture toughness and improve failure modes through crack deflection, fracture bridging, and frictional interface slip. Experimental observations show that ceramic composites initially fail at several points in the matrix and along the interfaces. These small cracks and inherent processing flaws propagate and coalesce, forming large cracks that lead to component failure. Therefore, an understanding of small crack growth is necessary for the design of composite systems which delay critical crack formation and which fail in a desirable manner.

The Surface Integral and Boundary Element Hybrid (SIBEH) method, supported by experimental observations, has been developed to model crack growth in brittle composite systems. The surface integral method models fractures as a piece-wise continuous distribution of displacement discontinuities. When combined with traditional boundary element methods, the technique provides an efficient tool for modeling three-dimensional crack growth.

This approach has been used to model matrix crack initiation in a lithium alumino-silicate (LAS) glass-ceramic that has been reinforced with continuous silicon carbide fibers. By modeling the effects of crack pinning and bridging, interfacial debonding, and frictional interface slip, this investigation aims to determine the stresses required for matrix crack initiation and the material parameters which promote 'graceful' failure modes. These results have been compared to existing analytical solutions for small crack growth. Results of this investigation are expected to be useful in developing guidelines for the manufacture and design of ceramic materials for high-temperature structural applications.

Thesis Supervisor: Michael P. Cleary
Title: Adjunct Professor of Mechanical Engineering

Acknowledgements

I am indebted to the Air Force Office of Scientific Research for funding my education and for sponsoring this research project through the Laboratory Graduate Fellow Program and Grant No. AFOSR-89-005. Dr. Alan Burkhard's personal mentorship and the management of Professort W.D. Peele are greatly appreciated.

Special thanks are due my family of friends and relations who have provided encouragement, guidance, and support throughout my tenure at M.I.T. Successful completion of my thesis research and doctoral degree would not have been possible without their help. Professor Cleary has provided direction and support for my research and teaching interests while allowing me freedom to explore and learn. For helping me navigate the sea of bureaucracy, I thank the staff of the department, including Leslie Regan, Joan Kravit, Susan Melillo, Lucy Piazza, Marie Pommet, Maureen DeCourcey, and John O'Brien.

For their help preparing for qualifying exams, I am indebted to Ashok Patel, Dale Watring, and John Wlassich. I also am grateful for the guidance and insightful suggestions of Professors Bill Keat, Michael Larson, D.M. Parks, J.J. Connor, and J.W. Hutchinson. Finally, I would like to thank the members of R.E.L. - most notably Tim Quinn - for years of support and friendship. This thesis would not have been possible without their daily support and laughter.

In spite of the distance involved, I have benefited from the love and friendship of my immediate family, including my sister, Ketti, my grandparents, and my fiancee, Kelly. This thesis is dedicated to my parents, Chuck and Sandie, for inspiring me - by example - to greater personal and professional heights. For this love and support I am eternally grateful.

Table of Contents

List of Figures

List of Tables

Chapter 1
Introduction

This investigation provides a fully three-dimensional analysis of small matrix crack growth in brittle materials reinforced with continuous brittle fibers for use in high-temperature structural applications. The project focuses on the influence of the fiber-matrix interface on small matrix crack growth and on fiber failure and is intended to supplement existing models by assessing the three-dimensional and bimaterial effects. Although the approach developed is general, a particular composite system consisting of lithium alumino-silicate (LAS) reinforced by silicon carbide fibers has been modeled to facilitate comparison with experimental data and existing models. A modified analytical expression is suggested for crack initiation and subsequent propagation.

1.1 Ceramics as Structural Materials

Ceramics are attractive structural materials because they offer high specific strengths, excellent thermo-mechanical properties, chemical and environmental stability, and low raw material costs [1]. For high-temperature applications, such as internal combustion engines for automotive and aeronautical propulsion, the use of ceramics offers great gains in efficiency because of their insulating properties and low thermal expansion coefficients. In many proposed applications (e.g. aerospace propulsion systems and alternate-cycle nuclear reactors), ceramics are the only possible material choice due to extreme operating temperature requirements. In spite of these demands,

ceramic materials have found limited use in critical structural applications due to their inherent brittle failure modes and notch sensitivity.

In the spirit of Griffith's brittle fracture investigations, research efforts aimed at improving the reliability of structural ceramics have shifted in focus from flaw control (i.e. minimizing the processing flaw size and density) to damage tolerance (i.e. improving the material's resistance to existing flaws). The recognition of resistance curve behavior in zirconia and the development of high-temperature reinforcing fibers sparked this shift and has renewed interest in structural ceramics designed for toughened fracture behavior. Subsequent experimental investigations and theoretical models have identified the primary toughening mechanisms and quantified many of their effects [2].

These dominant toughening mechanisms are depicted in Figure 1.1 and include transformation toughening, microcracking, and reinforcement by ductile or brittle inclusions. The first two are process-zone mechanisms which contribute stress-induced, volumetric dilation or softening (respectively) in the region of the crack tip and act to shield the flaw from the imposed global stress state. These mechanisms contribute modest gains in overall material toughness [2,3].

Additional gains in toughness can be achieved through bridging mechanisms, which transfer a portion of the applied load to intact inclusions spanning the fracture opening. This load 'shedding' acts to reduce the stress concentrations at the crack tip and is accomplished through shear stresses acting across bonded or frictionally constrained fiber/matrix interfaces. Ductile bridging of the fracture by bonded metallic particles can enhance toughness significantly but is limited to lower temperature ranges by the melting point and chemical reactivity of the inclusion [3]. Whisker or particle reinforcement by brittle inclusions also results in improvements in material toughness (roughly 200-300%) and offers higher operating temperature ranges [2].

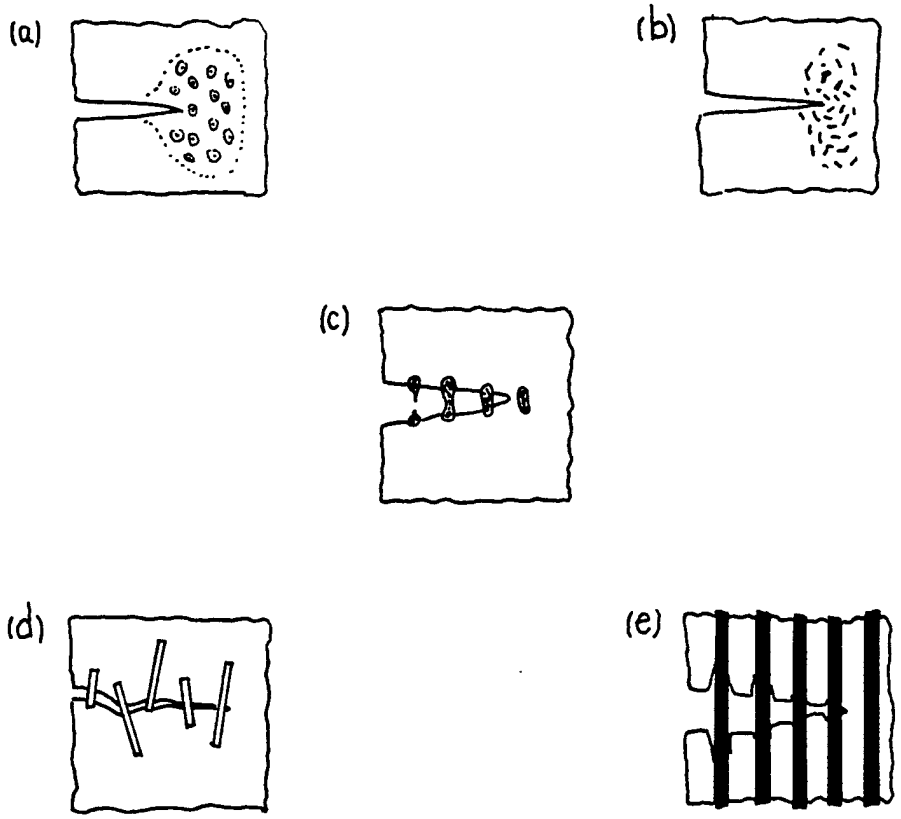

Figure 1.1 Dominant Toughening Mechanisms for Ceramic Materials; Dominant toughening mechanisms for brittle ceramic materials include (a) transformation toughening, (b) microcracking, (c) ductile reinforcement, (d) brittle whisker reinforcement, and (e) brittle fiber reinforcement.

The most significant increases in toughness can approach two orders of magnitude and are realized through continuous fiber reinforcement. Although it presents formidable manufacturing challenges, the incorporation of brittle fibers also offers material designers opportunities for damage tolerant behavior and more 'graceful' failure modes. In addition to the stress relief described above, local nonlinear effects such as debonding and frictional slip along fiber/matrix interfaces can contribute to the overall material toughness [1,2]. The strong influence of interfacial properties on these toughening mechanisms has

been demonstrated and suggests tremendous opportunities for designing ceramic materials. However, tailoring of the interface for toughened behavior remains the single greatest challenge for successful development of ceramic composites.

1.2 Failure of Fiber-Reinforced Ceramics

1.2.1 Damage Development

While little toughening occurs during the initial stages of damage development, this process has a significant impact on the final failure mode and on the toughening mechanisms available. Experimental observations show that 'large' matrix cracks (i.e. fractures that span many fibers) initiate from manufacturing flaws in the matrix that are typically on the order of the fiber spacing [4,5]. These small cracks propagate under applied loads and coalesce, forming large fractures which eventually lead to component failure [6,7].

Theoretical investigations of fracture growth in fiber-reinforced ceramics in which the fiber and matrix are firmly bonded have shown that the stresses imposed on the fiber by the crack tip are magnified significantly during small crack growth [8-10]. These local stresses pose a risk to the integrity of the fibers and therefore to the toughened failure modes which rely on them. To isolate the fibers from this stress concentration and avoid early fiber failure, the interface must be sufficiently weak. Unfortunately, this isolation also reduces the effectiveness of toughening and crack pinning mechanisms [7].

For these reasons, an understanding of the behavior of small crack growth in ceramic materials reinforced with frictionally-constrained fibers is required to balance these competing effects and to properly tailor the interface for toughened behavior. The results of this investigation are expected to provide structural engineers with the necessary tools to evaluate the integrity of ceramic composite components and to provide

material scientists with an understanding of how interfacial effects affect the overall composite behavior.

1.2.2 Failure Modes

The ultimate failure of composite material systems is complicated by fiber reinforcement, but has been categorized by Luh and Evans according to the macroscopic fracture behavior. These failure mode classes (Depicted in Figure 1.2) can be distinguished by the progression of constituent damage and are dependent on the relative structural properties - predominantly the fiber strength and interfacial shear strength [7].

When the failure strain of the fibers is less than that of the matrix or when defects are induced in the fibers during processing, the failure mode is dominated by frictional pullout of the remaining intact fiber segments under interfacial shear stress. In this case, the composite fails in a manner similar to ceramics reinforced with high aspect-ratio whiskers and the toughness increase ΔK is governed by the interfacial shear stress, τ, and the average pullout length, l. Even when the matrix fails preferentially, fiber failure can occur if the load transferred to the fibers as the matrix fractures exceeds the fiber strength. In this case, progression of the dominant matrix fracture is followed closely by fiber failure as the strong interfacial bonding transfers excessive loads from the failed matrix to bridging fibers in the crack-tip wake. While both of these modes can exhibit increased toughness, the composite remains notch sensitive and fails in catastrophic manners.

Only when the failure strain of the matrix is lower than that of the fibers and the fibers are sufficiently strong to support the stresses transferred from the matrix does the ceramic exhibit notch insensitivity and fail in a 'graceful' manner. In this case - depicted in Figure 1.2(c) - damage development occurs according to the process described above in Section 1.2.1, leaving a matrix riddled with cracks, but supported by intact fibers.

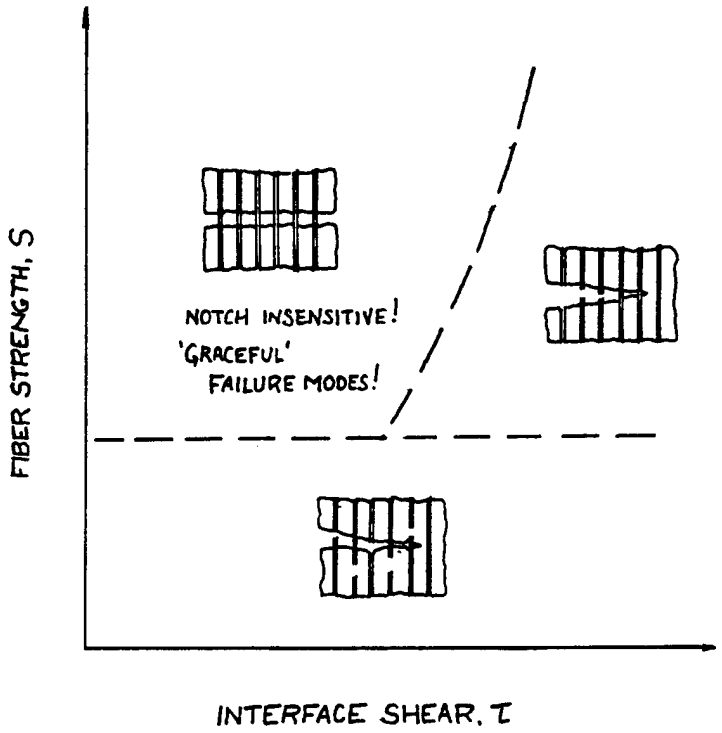

Figure 1.2 Failure Mode Map Failure of brittle ceramics reinforced with continuous brittle fibers is complicated, but can be classified according to the macroscopic fracture behavior. These failure modes are dependent on the constituent microstructural properties - predominantly the ultimate fiber strength, S, and the interfacial shear stress, τ. (Adapted from Reference [7])

More importantly, the composite may continue to support imposed loads in spite of extensive damage until the defects can be detected during regularly scheduled maintenance operations.

It is worth noting that the situation depicted in Figure 1.2 is further complicated by environmental factors (e.g. oxidation, irradiation), material changes (e.g. crystal growth in fibers), and stochastic manufacturing defects. All of these effects can

significantly influence the composite behavior, but are not accounted for in analytical fracture models.

1.2.3 Large Crack Models

Experimental evidence and theoretical models show that 'large' matrix cracks (i.e. fractures which span several fibers) bridged by intact fibers propagate at a cracking stress which is independent of crack length. Analytical models based on fracture mechanics and on energy considerations have been developed for these fractures and show good agreement with experimental data [11-17]. Commonly used models include those derived by Aveston, Cooper, and Kelly (ACK), by Budiansky, Hutchinson, and Evans (BHE), and by Marshall, Cox and Evans (MCE) [12,13,15]. These theories simulate the dominant toughening mechanisms which occur at this scale - fiber bridging and frictional interface slip - by applying uniform distributed closure pressures to an unbridged fracture model.

The ACK model predicts the steady-state matrix cracking stress, $\sigma_c^{(ACK)}$, as a function of the microstructural composite properties:

$$\sigma_C^{(ACK)} = E_C\left\{\frac{12\tau\gamma_m E_f V_f^2}{E_C E_m^2 R V_m}\right\}^{\frac{1}{3}} \tag{1.1}$$

In Equation (1.1), E_c represents the composite modulus ($E_mV_m+E_fV_f$) calculated using the elastic moduli, E_m and E_f, and volume fraction, V_m and V_f, of the constituent materials. The fiber radii, R, critical interfacial shear stress, τ, and the surface energy of the matrix material, γ_m, also influence the matrix cracking stress. Similar results are obtained using the BHE and MCE models.

1.2.4 Small Crack Models

Large crack models have been extended or adapted to estimate the stress required to initiate and to propagate small cracks [15-17]. However, as the fracture size decreases so does the appropriateness of the uniform corrective pressures applied in these models . In addition, small fractures may be subject to additional toughening mechanisms not significant for larger cracks (e.g. crack-tip pinning and frictional interface slip ahead of the fracture) [2]. The limits of applicability for these 'steady-state' models have been estimated to be several fiber spacings or greater. Meda and Steif have demonstrated the limited applicability for these fracture mechanics models when the radial fracture dimensions are less than the transition flaw size, c_t [18,19]:

$$c_t \approx 2c_n$$

$$\text{with } c_n = \left[\frac{R^2 E_c^4 K_{IC}^2}{4\pi^5 \tau^2 (1-\nu^2)^2 V_f^4 V_m^2 E_f^2 E_m^2} \right]^{1/3} \tag{1.2}$$

In Equation (1.2) K_{IC} is the critical mode I stress-intensity factor for propagation of bridged matrix flaws. This estimate is based on comparison of distributed spring models with the more simplistic long-crack models when the matrix cracking stress is within 50% of the ACK cracking stress. The transition flaw size can be significantly higher than this if closer agreement is required.

The acknowledged disadvantage of these models is that they do not accurately capture the toughening mechanisms that occur at this level, including the stiffening effects of fibers near and ahead of the fracture tip, the influence of interfacial sliding in this region, and the three-dimensional nature of the material and crack propagation. Further, these models make no estimate of the load transferred to the fibers or of the local

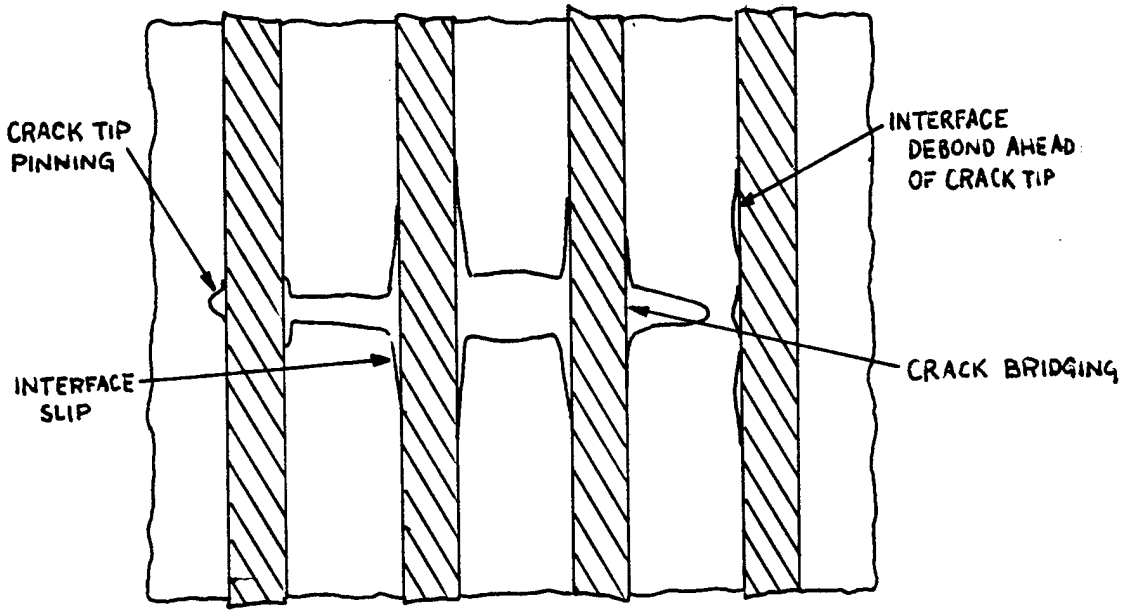

Figure 1.3 Small Matrix Crack Toughening Mechanisms; The influence of crack pinning by proximal fibers and interfacial slip ahead of the crack-tip can be significant for small matrix fracture propagation.

stress concentration in the fibers due to the proximal crack tip and transferred across the frictional interface.

These mechanisms have been investigated individually in detail, beginning with the two-dimensional work by Cook and Gordon [20]. Subsequent studies have captured new aspects of the problem, including line-tension models [21-23], computational investigations [8,10,24-27], and experimental efforts [22,28].

Several analytical models have been developed to estimate the matrix cracking stress for small crack growth subject to these toughening effects and are plotted in

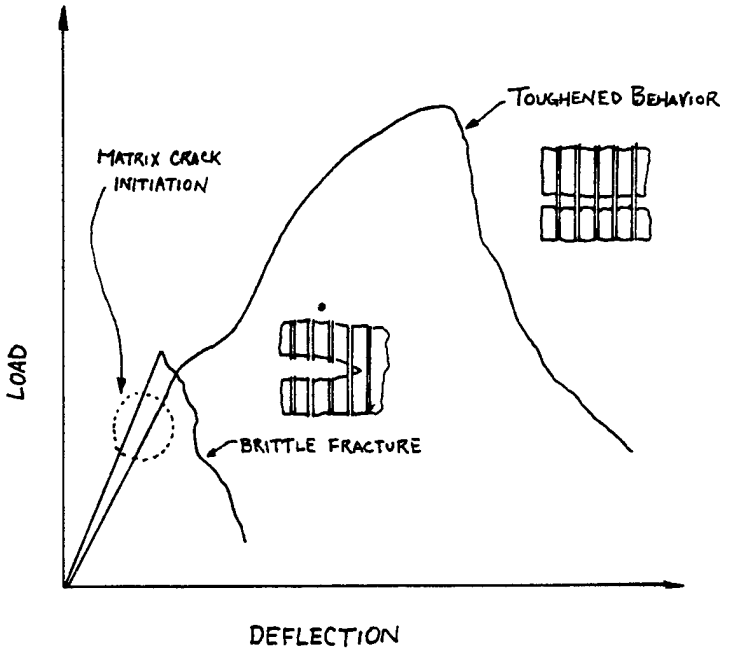

Figure 1.4 Toughened Ceramic Composite Load-Deflection Behavior; Experimental observations show that matrix fracture growth begins well before the onset of visible nonlinearity in the loda-deflection curce [4].

normalized form in Figure 1.5. Marshall, Cox, and Evans derive the following form based on a distributed-spring model [15]:

$$\frac{\sigma}{\sigma_c} = \frac{1}{3}\left(\frac{c}{c_m}\right)^{-1/2} + \frac{2}{3}\left(\frac{c}{c_m}\right)^{1/4} \tag{1.3}$$

$$\text{where } c_m = \left(\frac{\pi}{4(2/3)^{1/3}}\right)\left[\frac{K_{IC}V_m E_c R}{\tau V_f^2(1-\nu^2)E_f}\right]^{1/3}$$

Similar results have been obtained by McCartney and are included in Figure 1.5 [16].

The effects of these models have been simply summarized by Spearing and Zok in the following relation [29]:

$$\frac{\sigma}{\sigma_c} = \begin{cases} \left(\frac{a}{a_0}\right)^{-1/2} & \frac{a}{a_0} < \frac{1}{10} \\ \left(\frac{a}{a_0}\right)^{-1/4} & \frac{1}{10} \le \frac{a}{a_0} < 1 \\ 1 & \frac{a}{a_0} \ge 1 \end{cases} \qquad (1.4)$$

$$\text{with } a_0 = \frac{4\gamma_m V_m E_c}{3\sigma_c^2}$$

Meda and Steif have further improved upon these relations for intermediate length fractures and bridged the gap between the small crack and the steady-state crack models using an axisymmetric model with volume-weighted effective fiber properties [18-19]. Their theory links the matrix regions on opposing edge of the 'fiber' to simulate the connection which exists in three-dimensions. Although no explicit relation is given for the penny-shaped fracture, normalized results are included in Figure 1.5.

1.4 Research Scope

This investigation aims to contribute understanding of the influence of three-dimensional and bimaterial aspects of the problem on small matrix crack behavior using computational fracture mechanics. The focus of this investigation is accurate determination of the matrix cracking stress for small fractures in a stiffened, three-dimensional environment and investigation of the influence of the interface properties on the fiber stresses. Comparison of these results with existing solutions will provide some understanding of the three-dimensional and bimaterial effects which have been approximated in previous investigations.

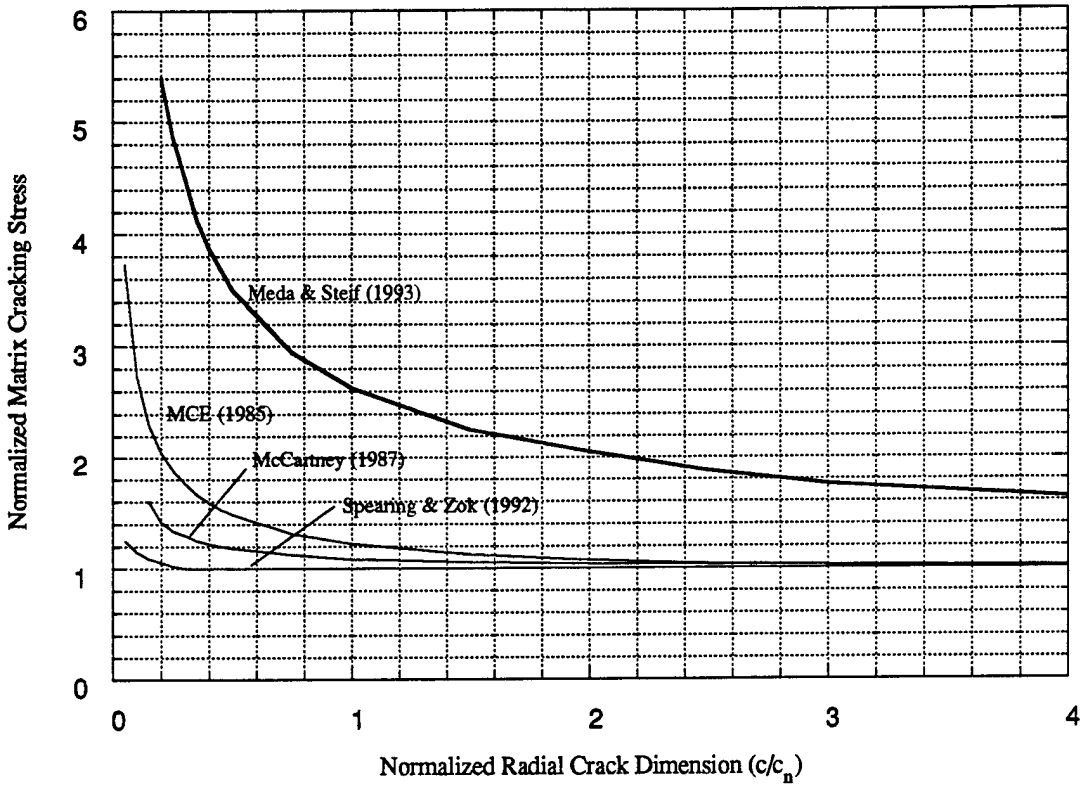

Figure 1.5 Matrix Cracking Stress Estimates for Small Fractures; Results of numerical and analytical models for matrix cracking stress in brittle composite materials are plotted as a function of the normalized characteristic radial crack dimension (c/c_n). The stresses have been normalized by the ACK steady-state cracking value.

Determination of the composite failure properties is accomplished by first developing an efficient computational scheme for fracture analysis in composite media. This technique is based upon the surface integral method, which models three-dimensional fractures in infinite media and was initially developed for hydraulic fracture applications [30]. The surface integral method is combined with traditional boundary element methods using superposition to incorporate the effects of model boundaries and stiffening fibers. For analysis of uniaxially reinforced composite materials, fracture cells are constructed on various scales to accurately model both crack initiation and small crack growth. Results generated include the matrix-crack stress intensity factors, applied

load, interfacial sliding work and areas, and the elastic input energy. The results of this investigation suggest modifications of existing crack theories for small crack growth.

1.4.1 Silicon Carbide/ Lithium Alumino-Silicate System

Although the approach is general, a particular composite system consisting of lithium alumino-silicate (LAS) reinforced with silicon carbide fibers will be modeled. This particular material has been chosen to facilitate comparison of results with experimental data and observations [4,6,7]. Lithium alumino-silicate is a glass-ceramic consisting of small crystal particles ranging from 0.05 to 1 micrometers in size surrounded by residual glass phase. The material is particularly well-suited for application to ceramic composites because of its low porosity, ease of formation, and small crystals. LAS fractures primarily by grain boundary cleavage or by separation of grain clusters and can operate at temperatures slightly above 1000° C [3,7,31].

The reinforcing fibers are silicon carbide fibers and are usually formed by deposition of a reactive ceramic on a fine tungsten core. The result is a fiber approximately 15-20 micrometers in diameter with low second-order crystallinity. Although their small size gives them flexibility necessary for processing, these 'tows' can be affected by exposure to high-temperatures and irradiation because of the manufactured microstructure [3,31].

1.4.2 General Assumptions

Several general assumptions have been made for this investigation involving aspects of the model. Both the matrix and fiber materials have been modeled as linear-elastic, isotropic materials. Although the matrix material is subject to limited plastic effects, including creep deformation and microcracking, these effects are assumed to be localized so that linear -elastic fracture mechanics is applicable. Although the relative

significance of these effects will increase with decreasing model scales, this investigation will provide a basis from which to evaluate the effects. The small particle size and amorphous structure of the matrix and fiber (respectively) suggest that this assumption is valid, though it may not be true for ceramics in which the grain size approaches the fiber spacing or in which the fiber crystal structure is well defined.

The interface between the fiber and matrix has been modeled - for simplicity - as having no thickness and subject to constant shear stress sliding. The assumptions are justified in that the interface slip captures the effects of the interphase and that any mechanical effects of the interphase can be incorporated into the fiber model. Although theoretical analysis has demonstrated the important influence of the normal stress in interfacial sliding on push-out tests, experimental evidence for these particular materials suggests that the constant shear stress model is sufficient since the interface is frequently under tension or separated slightly [7,32-34]. In addition, the effects of thermal expansions can be significant, but have not been included in this initial investigation [7]. These factors may be included in the model during future investigations.

1.4.3 Model Development and Results Presentation

The development and analysis of this matrix crack model are presented in the following chapters. Chapters 2 and 3 outline the development of the surface integral and boundary element hybrid method for application to three-dimensional fracture analysis in composite media. Chapter 2 outlines the fundamental theory used to derive the surface integral method, presents this fracture model in its current formulation and demonstrates its capabilities for modeling three-dimensional fractures in infinite media. A general integration scheme and error estimator utilized in this investigation are presented as well.

To evaluate the influence of composite fibers on small matrix crack growth, the surface integral method presented in Chapter 2 is combined with classical boundary

element methods using superposition. This chapter develops this hybrid technique in its current formulation. After briefly reviewing the fundamentals of the boundary element technique, Chapter 3 emphasizes the modeling features relevant to composite fracture mechanics, including boundary conditions, subregions, and interfacial slip zones.

Further details of the underlying theory and of the current implementation for both computational schemes are outlined in the Appendices A and B.

The application of the computational approach to matrix crack initiation and subsequent propagation is presented in Chapter 4. Verification of the routine by comparison to small crack propagation experiments is described, followed by results for a fully three-dimensional analysis of small crack growth in silicon carbide fiber-reinforced lithium alumino-silicate subject to remote tensile stresses. Pertinent results are compiled and presented along with an assessment of the SIBEH method for computational fracture analysis.

Suggestions for modification of existing cracking stress models are included in Chapter 5 along with a discussion of the implications for the manufacture and design of ceramic composite materials .

Chapter 2

The Surface Integral Method

Computational fracture mechanics models based on force dipoles or displacement discontinuities can provide accurate and efficient crack solutions for linear elastic materials. For this investigation, one such technique - the surface integral method - is employed to capture the three-dimensional aspects of small matrix crack growth. This chapter develops this technique in its current formulation and demonstrates its capabilities. Additional details of the underlying theory and its implementation for matrix crack analysis are described in Appendices A and B respectively.

2.1 Surface Integral Fundamentals

The surface integral method models three-dimensional fractures in linear elastic materials as a piece-wise continuous distribution of displacement discontinuities. This technique derives from the general concept that local material phenomena can be efficiently modeled with dipole distributions and resembles the indirect boundary element analysis in formulation [35,36]. Development of this computational scheme has been motivated by the need for efficient crack growth models which rely on accurate fracture parameter solutions and simplified growth logistics. Although originally developed for hydraulic fracture applications, the surface integral method has been used successfully to model arbitrary two- and three-dimensional crack growth in engineering materials, shear

band formation in granular media, and interfacial slip in composite materials [26,30,37-42].

The governing integral equation expresses the stress state in the material surrounding the crack as a function of the displacement discontinuity distribution:

$$\mathbf{t}(\mathbf{x}) = \mathbf{n}\int_{S_C} \gamma^s(\mathbf{x},\zeta)\delta(\zeta)\mathbf{dA}_\zeta \tag{2.1}$$

where $\mathbf{t}(\mathbf{x})$ represents the traction components at some point $\mathbf{x}$ with normal direction $\mathbf{n}$ in the media surrounding the fracture surface, S_C. The integrand combines the crack-face displacement distribution, δ, and a fundamental solution γ^s, which gives the stresses due to unit opening of an infinitesimal tensile or shear crack [35].

The influence functions γ^s, on which the method is based are derived by differentiation and combination of elasticity solutions for point forces acting in an infinite homogeneous medium [43]. In this formulation, an infinitesimal tensile crack is represented by a combination of dipoles as shown in Figure 2.1(a). The dominant dipole simulates the tensile crack opening, whereas the additional dipoles are included to counteract the associated Poisson contraction. A corresponding multipole can be constructed for the infinitesimal shear crack opening and is depicted in Figure 2.1(b) [35].

2.2 Discrete Formulation

For many practical applications an analytical representation for the crack-face displacements cannot be obtained. Therefore, the exact distribution is approximated in a piece-wise manner by dividing the crack surface into subregions over which some locally continuous distribution is assumed. As in classical boundary element methods, the estimated local distribution, $\delta^e(\zeta)$, is defined by the crack-face displacements at specific points within each element, δ^α, and shape functions, $N^\alpha(\zeta)$ [40]. In this formulation the

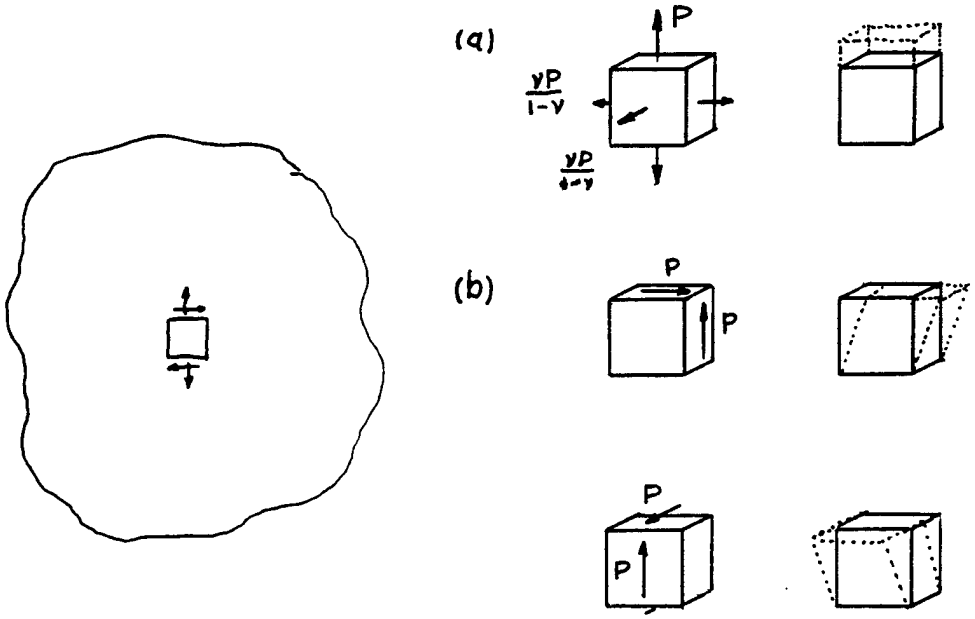

Figure 2.1 Tensile and shear displacement discontinuity representation; (a) and (b) depict the dipole combinations used to represent infinitesimal tensile and shear fracture events respectively. In (a), the dominant tensile dipole is supplemented with perpendicular dipoles to counteract Poisson contraction. In (b), the shear dipoles are balanced for moment equilibrium. Both are expressed as displacement discontinuities by combination with appropriate material parameters. (Adapted from Reference [35])

integral relation in Equation (2.1) becomes a summation of integrals taken for each elemental region, S_e, comprising the fracture surface.

$$\mathbf{t}(\mathbf{x}) = \sum_e \mathbf{n} \int_{S_e} \gamma^s(\mathbf{x},\zeta)\delta^e(\zeta)dA_\zeta \tag{2.2}$$

$$\text{where} \quad \delta^e(\zeta) = \sum N^\alpha(\zeta)\delta^\alpha \tag{2.3}$$

To determine the crack-face displacement distribution, a collocation method can be employed in which the applied boundary conditions are enforced at a distinct number

of points (collocation points) on the crack surface [38.35]. This results in a linear system of equations relating the crack-face displacements and tractions:

$$\mathbf{C_{IJ}}\delta_J = \mathbf{t_I} \tag{2.4}$$

$$\text{where} \quad \mathbf{C_{IJ}} = n\int_{Se^{(J)}} \gamma^s(\mathbf{x}_p,\zeta)N^{(J)}(\zeta)dA_\zeta \tag{2.5}$$

The coefficient matrix terms $\mathbf{C_{IJ}}$ represent the traction forces $\mathbf{t}$ at collocation point I corresponding to unit crack-face displacements δ at collocation point J. The integration in Equation (2.5) is taken over the elements $S_e^{(J)}$ enclosing point J.

The linear system expressed in Equation (2.4) can be solved, and the results can be combined with prescribed shape functions to obtain the approximate crack opening distribution. Stresses and displacements at points in the surrounding media can then be expressed as a function of the crack-face displacement distribution:

$$\mathbf{t}(\mathbf{x}) = \sum \delta^J n\int_{Se^{(J)}} \gamma^s(\mathbf{x},\zeta)N^{(J)}(\zeta)dA_\zeta \tag{2.6}$$

$$\mathbf{u}(\mathbf{x}) = \sum \delta^J n\int_{Se^{(J)}} \gamma^d(\mathbf{x},\zeta)N^{(J)}(\zeta)dA_\zeta \tag{2.7}$$

where γ^d in Equation (2.7) represents the fundamental displacement solution giving the displacements at a point x in the elastic medium surrounding an infinitesimal fracture event.

In general, the integral terms in Equations (2.5-2.7) can be handled using two-dimensional Gaussian quadrature. However, when the collocation points at which the tractions and prescribed crack openings are evaluated coincide, the $1/\mathbf{R}^3$ singularity of the fundamental stress solution makes the integral intractable. Even for cases of a proximal sampling point (important for the hybrid concept developed in Chapter 3),

purely numerical integration with reasonable integration orders is often corrupted with significant computational errors.

For planar crack elements with internal collocation points, these situations can be efficiently handled by subtracting an integral term equivalent to a rigid body motion [35]:

$$C_{IJ} = n\int_{Se^{(J)}} \gamma^s (N^{(J)}(\zeta) - N_0^{(J)})dA + N_0^{(J)} n\int_{Se^{(J)}} \gamma^s dA$$

$$= n\int_{Se^{(J)}} \gamma^s (N^{(J)}(\zeta) - N_0^{(J)})dA - N_0^{(J)} n\int_{S_T - Se^{(J)}} \gamma^s dA + N_0^{(J)} n\int_{S_T} \gamma^s dA \quad (2.8)$$

where $N_0^{(J)}$ is the shape function value at the singular collocation point and S_T represents the entire fracture plane.

The first integral in Equation (2.8) is now defined in the sense of a Cauchy principal value and can be computed directly. The third term represents a rigid body motion of the entire fracture plane and contributes a finite value to either the stress state (no contribution) or to the displacements (N_0). Evaluation of the second integral term is somewhat more complicated but can be accomplished by first recognizing that the individual terms of the fundamental solutions are products of radial terms, $\gamma_R(r,z)$, and angular terms, $\gamma_\theta(\theta)$, when expressed in a local cylindrical coordinate frame. In this form, the radial terms can be integrated analytically. The remaining angular integrals are then evaluated with one-dimensional Gaussian quadrature.

$$\gamma(x,\zeta) = \sum \gamma_\theta(\theta)\gamma_R(r,z) \quad (2.9)$$

$$\int \gamma(x,\zeta)dA = \int \gamma_\theta(\theta) \int_{r(\theta)}^{\infty} \gamma_R(r,z) r dr d\theta \quad (2.10)$$

In research conducted independently, this integration approach has also been applied successfully to regularized integrals for the boundary element method [44].

Despite these complicated integration procedures and its limitation to linear elasticity, the surface integral method provides several advantages over conventional numerical techniques. Because the fundamental equations are based on multipole solutions (representing infinitesimal fracture events), the surface integral technique accurately captures the stress singularities near the crack tip. Crack-face displacements and stress intensity factors can be determined with a limited number of low-order crack elements [40].

More importantly, only the fracture surface is discretized, which reduces the required degrees of freedom and simplifies crack growth logistics. Extension of the fracture surface to simulate crack propagation simply involves the addition of elements and periodic surface remeshing. This is a considerable advantage when compared to classical finite element methods, which require significant mesh refinement and frequent volumetric remeshing in the regions surrounding the propagating crack tip.

2.3 Current Implementation

The technique outlined above has been implemented for analysis of three-dimensional fractures in linear elastic media. Although the approach is valid for arbitrary crack geometries and boundary conditions, the model has been simplified for this investigation to planar matrix flaws subject to boundary conditions which are symmetric about the fracture plane (i.e. tensile crack opening only). Extension of the approach to more general situations is straightforward and has been presented [26,35].

To approximate the crack opening distribution, the fracture surface is subdivided into elemental regions over which local variation forms are prescribed. The fracture analysis code currently offers a variety of element configurations as outlined in Figures 2.2 and 2.3. Each fracture surface can be subdivided into three- and four-sided elemental

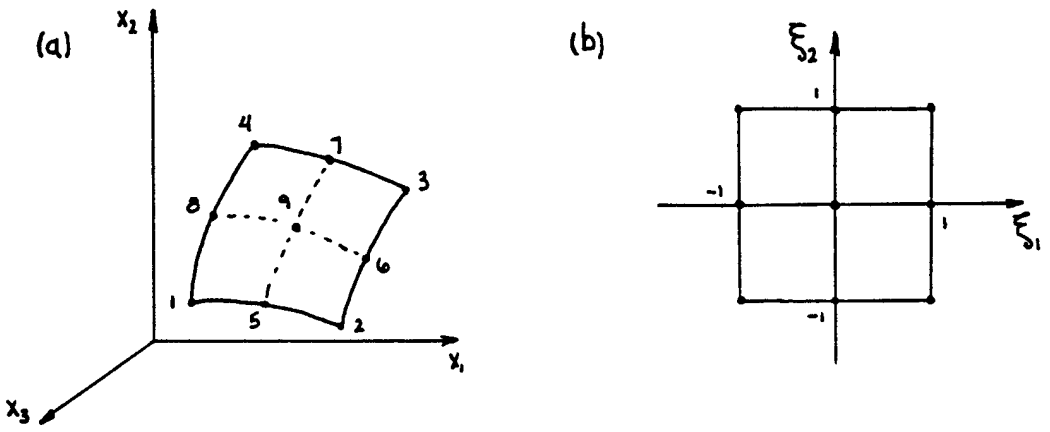

Figure 2.2 Nine-Noded Element Geometry; The fracture surface is subdivided into three- and four-sided elements with linear and parabolically curved boundaries. Mapping from the element reference frame (b) is based on the bi-quadratic Lagrange functions.

regions bounded by straight or parabolically curved boundary segments. For integration purposes, points on the elemental fracture surface, x_p, can be related to the local element reference frame, ξ, by the bi-quadratic mapping functions, $M^{\alpha}(\xi)$, from the Lagrange family [45].

$$x_p(\xi) = \sum M^{\alpha}(\xi) x^{\alpha} \tag{2.11}$$

Of course, simpler element geometries are possible but are included as specialized forms of this basic nine-noded Lagrange element.

The singularity of the fundamental stress solution precludes an isoparametric representation for the crack opening distribution except in very rigorous formulations

[10,36,46]. However, experience indicates that accurate fracture parameter and crack-face displacement solutions can be obtained with simpler local distributions [26,35]. Three basic shape functions have been found sufficient and are summarized in Figure 2.3. Implemented options include constant, constant-linear, and special crack-tip distributions. The approximate local crack opening is then given as a function of the crack-face displacements at internal collocation points, δ^α, and the prescribed elemental shape functions, N^α. Although the use of internal collocation points results in a discontinuous crack opening at the element boundaries, moderate mesh refinement significantly limits the extent of these discontinuities. In fact, this incompatibility serves as a useful error indicator as discussed in Section 2.5 below.

Accurate fracture parameter and crack-face displacement solutions rely on the use of special crack-tip elements for the crack periphery. The crack-opening distribution within these elements varies as a function of the distance from the crack tip according to the first two terms of the Williams expansion, $\rho^{1/2}$ and $\rho^{3/2}$ [47]. From this assumed variation, two elemental shape functions, $N^\alpha(\xi)$, can be derived in terms of displacement values at the internal collocation points [26],

$$N^1(\xi) = \frac{\rho_2^{3/2}\rho(\xi)^{1/2} - \rho_2^{1/2}\rho(\xi)^{3/2}}{\rho_2^{3/2}\rho_1^{1/2} - \rho_2^{1/2}\rho_1^{3/2}}$$

$$N^2(\xi) = \frac{\rho_1^{1/2}\rho(\xi)^{3/2} - \rho_1^{3/2}\rho(\xi)^{1/2}}{\rho_2^{3/2}\rho_1^{1/2} - \rho_2^{1/2}\rho_1^{3/2}} \qquad (2.12)$$

where $\rho(\xi)$ represents the distance from the crack tip, and ρ_1 and ρ_2 are the corresponding collocation point distances. In contrast with conventional formulations, the crack-tip shape functions depend on the actual crack tip radius and only indirectly on the local element coordinates.

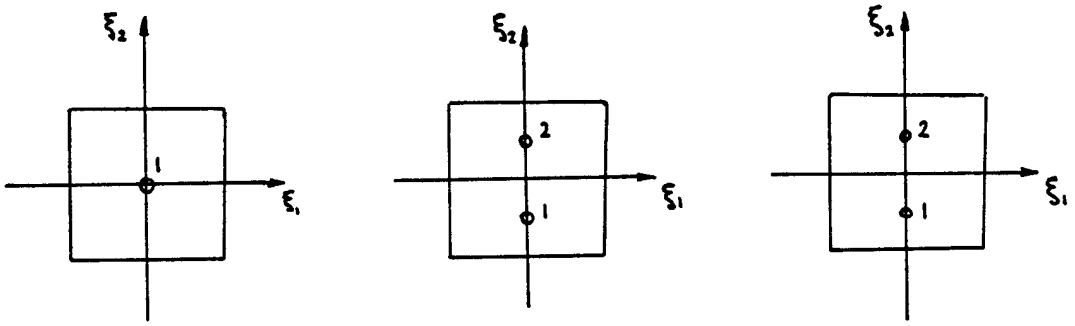

(a) Constant Element	(b) Linear Element	(c) Crack-Tip Element
$\delta(\xi) = \delta^1$	$\delta(\xi) = (\delta^1 + \delta^2)/2 + (\delta^2 - \delta^1)\xi_2$	$\delta(\xi) = f^1(\delta^1, \delta^2)\rho(\xi_2)^{1/2} + f^2(\delta^1, \delta^2)\rho(\xi_2)^{3/2}$

Figure 2.3 Summary of Element Shape Functions; Crack-face displacement distributions within an elemental subregion are defined as a function of the crack opening at internal collocation points and the prescribed shape functions. Constant, linear, and special crack-tip functions can efficiently approximate crack opening for general three-dimensional fracture situations.

More importantly, local stress-intensity factors can be accurately computed from the crack opening displacement at some small distance from the crack tip, ρ_0. For the tensile crack case [35]:

$$K_I = \frac{G}{(1-\nu)} \frac{\delta^e(\rho_0)}{2\sqrt{2\rho_0/\pi}} \tag{2.13}$$

2.4 Fracture Model Results

To demonstrate the capabilities of the surface integral method, crack-face displacement and stress-intensity factor solutions are presented for a variety of three-dimensional fracture configurations. Figures 2.4 and 2.5 show crack opening profiles superimposed on typical surface discretizations for penny-shaped and elliptical cracks (respectively) subject to uniform internal pressure. Table 2.1 shows the corresponding stress-intensity factors for selected points along the elliptical crack periphery.

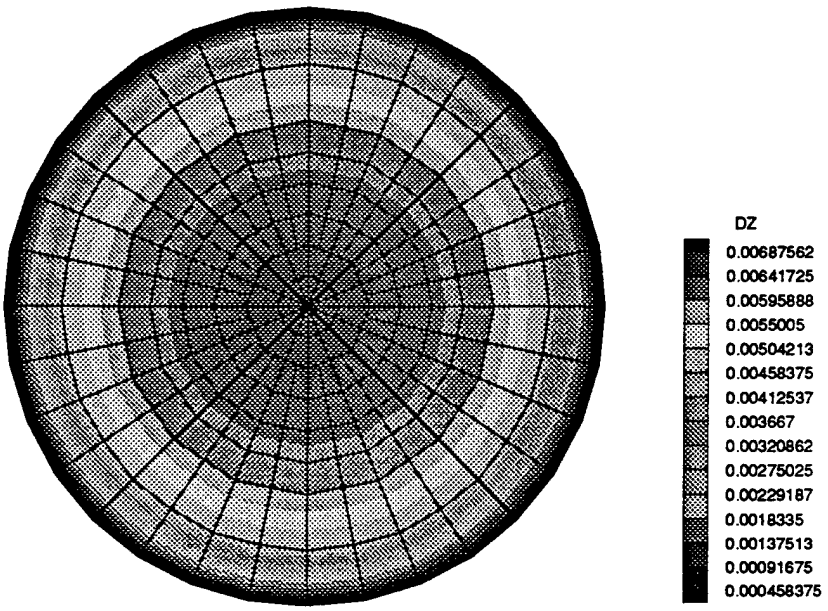

$$K_I^{(CALC)} / 1.128\sigma_\infty \sqrt{a} = 0.97$$

Figure 2.4 Penny-Shaped Crack Subject to Internal Pressure; Crack surface discretization and crack-face displacement contours are shown for a penny-shaped crack model subject to uniform internal pressure [47].

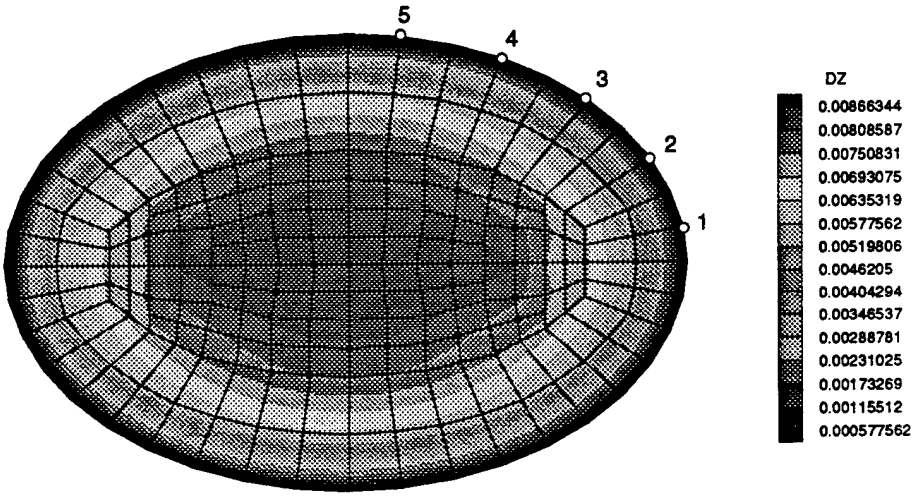

Figure 2.5 Elliptical Crack Subject to Internal Pressure; Crack surface discretization and crack-face displacement contours are shown for an elliptical crack model subject to uniform internal pressure. Stress-intensity factors have been estimated at the points shown and are tabulated below.

Table 2.1 Stress-Intensity Factors for Elliptical Crack; Calculated stress-intensity factors for selected points along the crack periphery show good agreement with analytical solutions [48].

Point:	$(K_I/K_o)_{CALC.}$	$(K_I/K_o)_{THEOR.}$	% Error
1	0.799	0.80	0.1
2	0.831	0.84	1.1
3	0.868	0.89	2.5
4	0.913	0.94	2.9
5	0.927	0.96	3.4

The robustness of both the method and the integration scheme is demonstrated by the remaining two fracture models. The first (Figure 2.6 and 2.7) involves two collinear penny-shaped cracks and demonstrates the method's capabilities for simulating multiple, interacting fractures.

For the second model, the fundamental solutions for a crack in an infinite homogeneous medium have been replaced by solutions derived for fractures along a bimaterial interface. These influence functions have been derived from elasticity solutions for a point force in one of two dissimilar, bonded, semi-infinite regions [43]. Although the analytically integrated terms were more complicated, the derivation follows the same approach used for the homogeneous case. Solutions for a wide range of material combinations show good agreement with analytical solutions (Figure 2.8).

2.5 Numerical Issues

In addition to the integration issues addressed above, several other numerical artifacts can significantly affect solution accuracy and convergence. These include the collocation point distribution, the prescribed local variation (e.g. shape function order, surface discretization), and the applied boundary conditions. In general, accuracy will improve with increasing collocation point density and uniformity, increasing shape function order, and decreasing variation in local boundary conditions. For efficient problem solution, crack surface discretization must be tailored to capture the local crack opening distributions. Meshing heuristics have been developed regarding relative element sizes and types by comparing a range of representative computational solutions with known analytical solutions.

In addition, an error indicator based on the discontinuity in estimated crack opening at the element boundaries has been employed here to supplement these

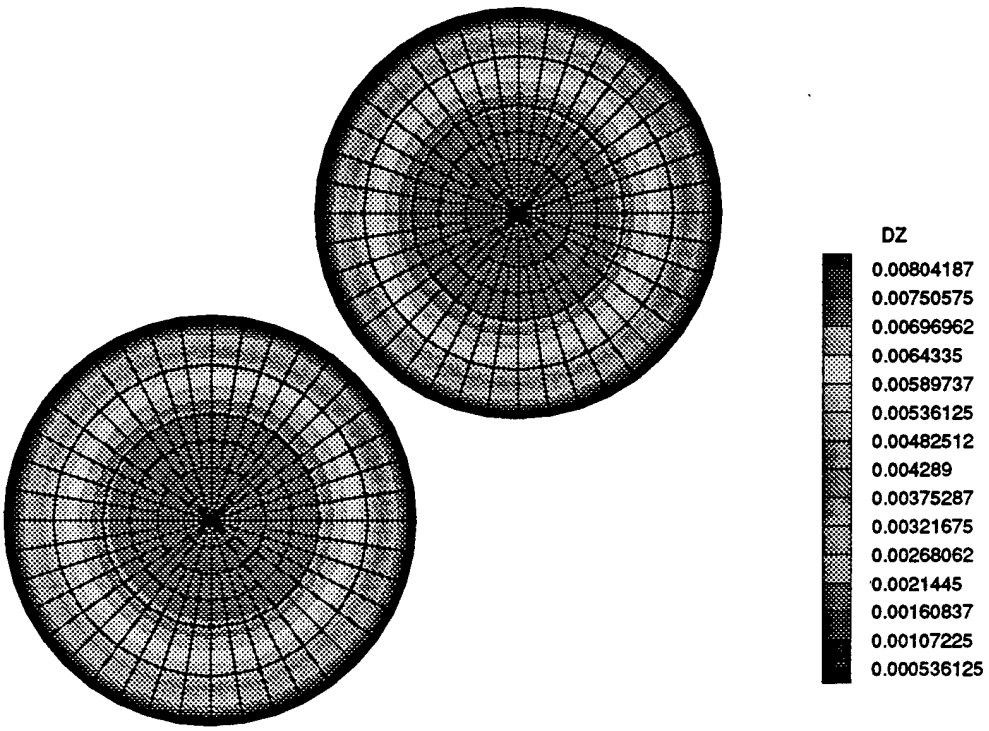

Figure 2.6 Collinear Penny-Shaped Cracks Subject to Internal Pressure; Crack surface discretization and crack-face displacement contours are shown for two collinear penny-shaped cracks subject to uniform internal pressure. Stress-intensity factors have been estimated at the points shown and are tabulated below [49].

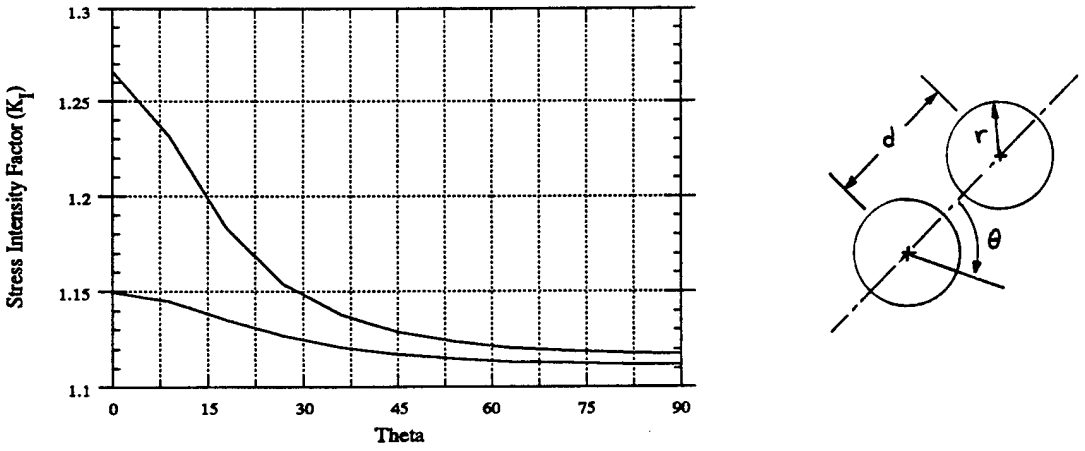

Figure 2.7 Stress-Intensity Factors for Collinear Penny-Shaped Cracks; Calculated stress-intensity factors are plotted as a function of the position along one crack periphery for two cases (r/d = 0.8 and 0.94).

predictive model definitions. To generate displacement distribution plots, the crack opening at the nodal points are estimated as a function of the surrounding elemental variations. Since these estimates can differ across element boundaries, the maximum difference as a fraction of the averaged value can be used as a qualitative error indicator [24]. Small relative discontinuities in the crack-face displacements indicate a sufficiently refined model, whereas large values can signal difficulties. Tests indicate that for stress-intensity factor estimates with less than 5% uncertainty, the local relative displacement discontinuity should be no larger than 20%.

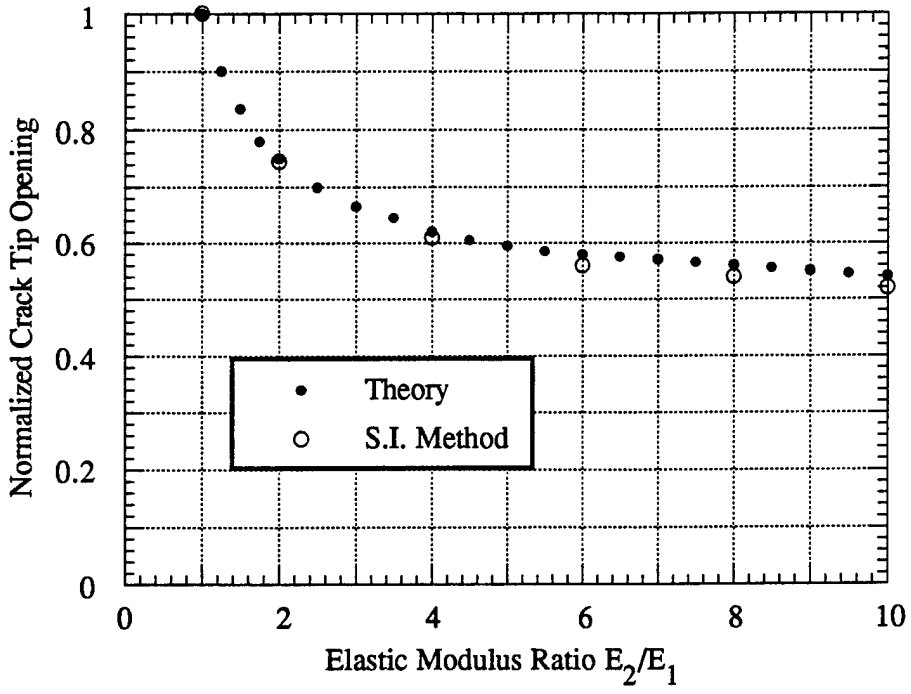

Figure 2.8 Calculated Crack Opening Displacements for Penny-Shaped Interface Flaws Subject to Internal Pressure; (normalized with respect to the homogeneous case) Crack opening solutions for a penny-shaped interface flaw subject to uniform internal pressure show good agreement with analytical predictions for a wide range of material combinations [50].

Chapter 3

The Surface Integral and Boundary Element Hybrid (SIBEH) Method

To evaluate the influence of composite fibers on small matrix crack growth, the surface integral method presented in Chapter 2 has been combined with classical boundary element methods using superposition. This chapter develops this hybrid technique in its current formulation. After briefly reviewing the fundamentals of the boundary element technique, Chapter 3 emphasizes the modeling features relevant to composite fracture mechanics, including boundary conditions, subregions, and interfacial slip zones. Further details of the underlying theory and of the current implementation are outlined in the appendices.

3.1 SIBEH Method Fundamentals

The effectiveness of the surface integral method for modeling three-dimensional fractures in infinite domains has been demonstrated. Previous investigations have combined the surface integral and finite element methods to model fractures in the presence of finite component boundaries, symmetric planes, material interfaces, contained crack-tip plasticity, and thermal strains [26,35,37-42]. These analyses have used the surface integral method for accurate fracture solutions and relied on the coupled finite element models to account for component and material effects. Successful

applications of this approach include hydraulic fracture for oil and gas recovery, crack growth in engineering materials, and thermo-elastic fatigue.

For the present analysis, the surface integral method has been combined with the boundary element method in a similar hybrid formulation (SIBEH). The matrix crack (surface integral) model has been superposed with boundary element models of the surrounding matrix and proximal fibers. Although it results in fully-populated, coupled coefficient matrices, this formulation avoids the complicated volumetric finite element meshes which would be required for this problem. In addition to the fracture surface, only the material interfaces, symmetric planes, and loading surfaces are discretized.

3.1.1 Elastostatic Boundary Element Model

The boundary element method can be derived as a 'weak' formulation of weighted residual statement for linear elastostatics [51,52]. The resulting integral equation (Somigliana's identity) expresses the displacements at a point, I, in the modeled region as a function of the traction and displacement distributions along the region bounds, Γ.

$$U_I(x) = \int_\Gamma u^*(x,x_p)T(x_p)dA_\Gamma - \int_\Gamma p^*(x,x_p)U(x_p)dA_\Gamma \qquad (3.1)$$

where u* and p* represent influence functions derived from elasticity solutions for a point force in an infinite, homogeneous domain. $T(x_p)$ and $U(x_p)$ represent the boundary traction and displacement distributions, respectively.

In practice, these distributions are approximated by dividing the model boundary into distinct elemental subregions over which some low-order distribution behavior is assumed. In this way, the tractions and displacements can be expressed in a piece-wise continuous fashion in terms of locally based distribution (shape) functions, $N^{(J)}$, and of the traction and displacement values at specific boundary (collocation) points, T_J and U_J.

$$T(x_p) = \sum N^{(J)}(x_p)T_J$$

$$U(x_p) = \sum N^{(J)}(x_p)U_J \tag{3.2}$$

Using these approximations, Equation (3.1) becomes:

$$U_I(x) = \sum T_J \int_\Gamma u^*(x,x_p)N^{(J)}(x_p)dA_\Gamma$$

$$-\sum U_J \int_\Gamma p^*(x,x_p)N^{(J)}(x_p)dA_\Gamma \tag{3.3}$$

Applying Equation (3.3) to each boundary collocation point results in a linear system of equations which can be used to solve general boundary value problems:

$$H_{IJ}U_J = G_{IJ}T_J \tag{3.4}$$

$$H_{IJ} = \delta_{IJ}c^{(J)} + \int_{Se^{(J)}} p^*(x_p^I,x_p)N^{(J)}(x_p)dA_\Gamma \tag{3.5}$$

$$G_{IJ} = \int_{Se^{(J)}} u^*(x_p^I,x_p)N^{(J)}(x_p)dA_\Gamma \tag{3.6}$$

where $c^{(J)}$ contains geometric constants dependent on the local boundary, and the integrations are taken over the region $Se^{(J)}$ surrounding the collocation point J.

Stresses at points within the model can then be expressed as a function of the applied boundary values, the associated solutions, and the derivative kernel functions d* and s* [51]. The traction force at a point in the model interior, t(x), for a specific normal direction, n, is given by the Equation (3.7):

$$t(x) = \sum T_J n \int_\Gamma s^*(x,x_p)N^{(J)}(x_p)dA_\Gamma$$

$$-\sum U_J n \int_\Gamma d^*(x,x_p)N^{(J)}(x_p)dA_\Gamma \tag{3.7}$$

Extension of these relations to include body forces, thermal strains, and contained plasticity is straightforward, but has been omitted from this derivation for clarity.

3.1.2 Hybrid Formulation

The process used to couple the surface integral and boundary element models combines the fundamental relations of each technique using superposition as depicted in Figure 3.1. The problem of a finite, fractured body under applied crack-face and boundary tractions (Figure 3.1(a)) can be solved directly by superposing and linking the two models as shown. Although the model discussed involves only traction boundary conditions, extension of the resulting relations to mixed boundary value problems can be accomplished simply by partitioning the coefficient matrices and rearranging terms.

The surface integral method, shown in Figures 3.1(b), models the fracture in an infinite homogeneous domain, whereas the boundary element model in Figure 3.1(c) handles the finite, uncracked component. This approach uses the accurate fracture modeling capabilities of the surface integral method to greatest advantage while retaining the generality of the boundary element method. The surface integral equation system is are constructed as before. However, corrective tractions, t^c, (evaluated along the image of the fracture in the boundary element model) must be subtracted from the applied tractions, t, to ensure satisfaction of the overall boundary conditions.

$$[C]\{\delta\} = \{t\} - \{t^C\} \tag{3.8}$$

These corrective tractions can be expressed in terms of the boundary element displacements and tractions.

$$\{t^C\} = [D]\{U^{be}\} - [S]\{T^{be}\} \tag{3.9}$$

where [D] and [S] represent the integrals expressed in Equation (3.7) and are evaluated at images of the surface integral collocation points in the boundary element model.

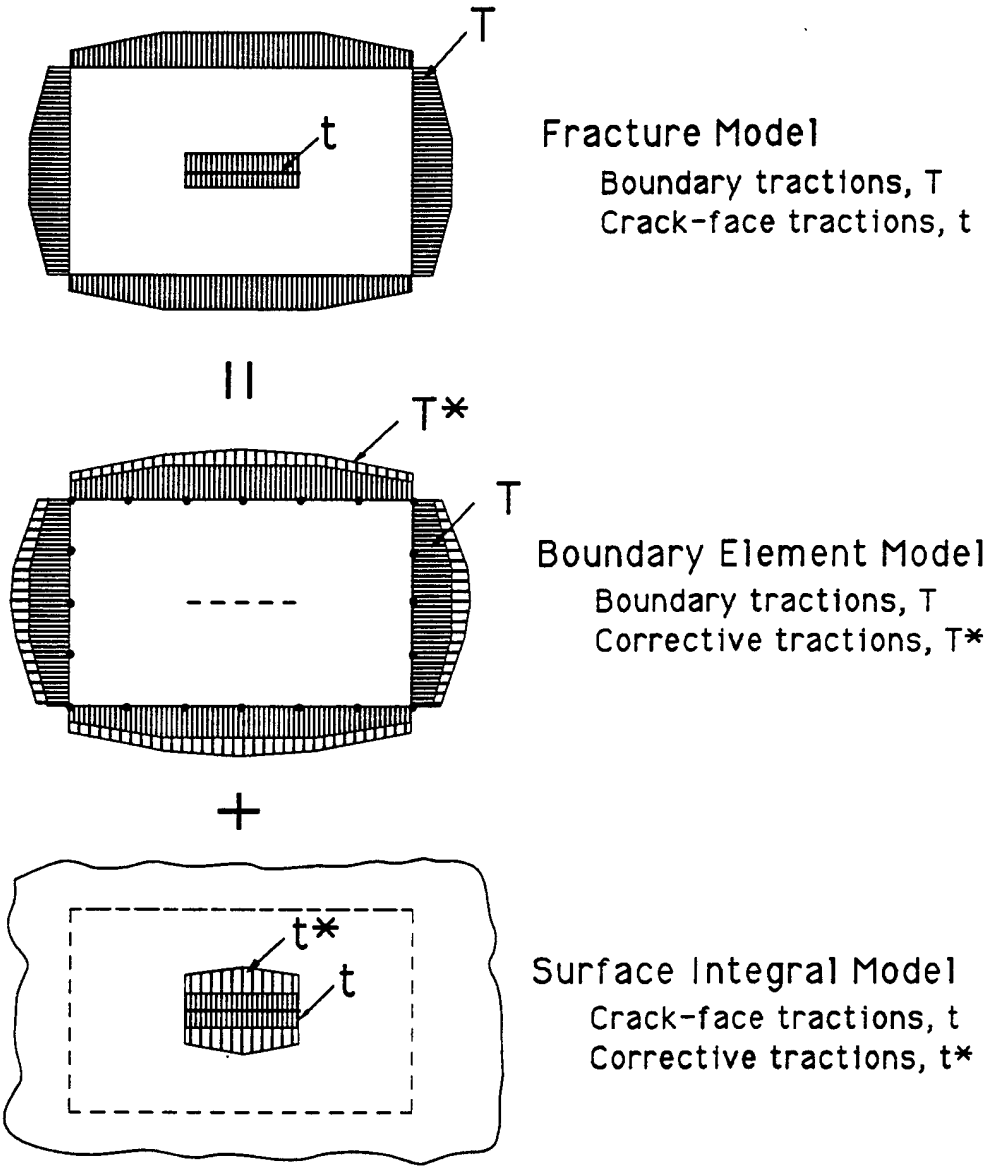

Figure 3.1 Superposition of Surface Integral and Boundary Element Models; To solve the problem of a finite, cracked body subject to applied crack-face and boundary tractions (a), the surface integral method fracture model (b) and the boundary element method component model (c) can be superposed and linked to ensure satisfaction of applied boundary conditions. Mixed boundary value problems can be solved as well simply by partitioning the resulting equation system and rearranging terms.

Similarly, satisfaction of the global conditions along the component boundaries is ensured by combining the applied tractions with corrective tractions from the surface integral model for points interior to the finite, uncracked model in Figure 3.1(c):

$$\{T^{be}\} = \{T\} - \{T^{C}\} \tag{3.10}$$

Using the integral relations in Equation (2.6), these corrective tractions can be expressed as a function of the crack-face displacements:

$$\{T^{C}\} = [J]\{\delta\} \tag{3.11}$$

In this case, the terms of matrix [J] are evaluated along the images of the boundary element collocation points in the surface integral model.

Equations (3.10) and (3.11) are applied to the boundary element integral relations for the model depicted in Figure 3.1(c):

$$\begin{aligned}[H]\{U^{be}\} &= [G]\{T^{be}\} \\ &= [G]\{T\} - [G]\{T^{C}\} \\ &= [G]\{T\} - [G][J]\{\delta\}\end{aligned} \tag{3.12}$$

However, displacements along the boundary of the original problem are a sum of the displacements from both superposed models, a distinction which is critical for mixed boundary value problems.

$$\{U\} = \{U^{si}\} + \{U^{be}\} \tag{3.13}$$

The displacements {Usi} are given by the matrix form of Equation (2.7) evaluated at the images of the boundary element collocation points in the surface integral model:

$$\{U^{si}\} = [L]\{\delta\} \tag{3.14}$$

Combining Equations (3.8)-(3.14) gives the complete hybrid method equation system, relating the crack-face and boundary displacements to the applied tractions.

$$\begin{bmatrix} C - DJ + SL & S \\ GJ - HL & H \end{bmatrix} \begin{Bmatrix} \delta \\ U \end{Bmatrix} = \begin{bmatrix} I & D \\ 0 & G \end{bmatrix} \begin{Bmatrix} t \\ T \end{Bmatrix} \tag{3.15}$$

By combining the fracture modeling capabilities of the surface integral method with the versatility of the boundary element method, the SIBEH method provides an efficient and robust tool for linear elastic fracture mechanics. The technique is particularly well suited for fracture propagation analysis since only a limited number of terms in Equation (3.15) need to be recomputed as the crack face is extended.

3.1.3 Multiple Region Models

To incorporate the stiffening effects of inclusions (e.g. fibers) in composite media, the hybrid formulation presented above can be extended using a subregioning approach common to boundary element analysis [51]. Additional regions, either cracked or intact, can be linked to the main model by enforcing displacement equality and traction continuity across the interface. For boundary values at corresponding interfacial nodes,

$$\mathbf{U}^1 = \mathbf{U}^2$$

$$\mathbf{T}^1 = -\mathbf{T}^2 \tag{3.16}$$

where the superscripts 1 and 2 denote the two bonded subregions. When solved directly, the resulting set of equations takes the form:

$$\begin{bmatrix} C-DJ+SL & S^1 & S_i^1 & -D_i^1 & \\ GJ-HL & H^1 & H_i^1 & -G_i^1 & \\ & & H_i^2 & G_i^2 & H^2 \end{bmatrix} \begin{Bmatrix} \delta \\ U^1 \\ U_i \\ T_i \\ U^2 \end{Bmatrix} = \begin{bmatrix} I & D^1 & \\ & G^1 & \\ & & G^2 \end{bmatrix} \begin{Bmatrix} t \\ T^1 \\ T^2 \end{Bmatrix} \tag{3.17}$$

where the partitions of each of the subregion equation systems have been combined according to the relations in Equation (3.16). Additional subregions can be combined by relating the boundary values at common interfacial nodes in a similar fashion. Although this system of equations can be used to accurately model composite media, this approach leads to a large proportion of zero terms, suggesting the existence of more efficient solving schemes.

3.2 Current Implementation

This hybrid approach has been implemented for analysis of small matrix crack growth in composite media with the capacity to model the fractured matrix and up to three additional particles or fibers. To establish the system of equations expressed above in Equations (3.15) and (3.17), the matrix and fiber surfaces are divided into three- and four-sided elemental regions bounded by linear or parabolically-curved boundaries. Points on the elemental boundary surface, $\mathbf{x}_p$, can be related to a local element reference frame using the bi-quadratic mapping functions described in Chapter 2:

$$\mathbf{x}_p(\xi) = \sum \mathbf{M}^{\alpha}(\xi)\mathbf{x}^{\alpha}. \tag{3.18}$$

For simplicity, lower order elements are modeled as reduced forms of these nine-noded Lagrange elements.

The singularities of the primary fundamental solutions u* and p* are weaker than those derived for the surface integral method by one order. Because of this difference,

singular integrals for points on element boundaries can be defined in a limiting sense and evaluated with specialized integration schemes. Therefore, the bi-quadratic mapping functions are also used to represent the local boundary value variations in Equations (3.2). This iso-parametric formulation permits continuous boundary value distributions and reduces the collocation point density required for accurate solutions. Use of the Lagrange family of functions leads to relatively uniform collocation point distributions and therefore more accurate solutions.

3.2.1 Singular Integration Scheme

Singular integrals occur regularly in the boundary element formulation when the source point and the element over which the fundamental solutions u* and p* are evaluated coincide. Many methods for evaluation of these singular terms have been proposed, including modified quadrature rules, element subdivision, analytical representations, and coordinate transformations [54-59]. The most elegant (and most accurate) integration scheme results in complete regularization of the integrand and can be applied to general, three-dimensional elastostatic elements [44]. This recently developed approach has been implemented for singular and near-singular integrals and is summarized here (Additional details can be found in Appendix B).

Using an approach similar to that presented for the surface integral method, the singular integrals are regularized by subtraction of a first-order Taylor series expansion of the integrand about the collocation point, Q, nearest to the source point, P. To facilitate semi-analytic integration of the regularizing terms, this integral is evaluated in a plane which is tangent to the element at Q.

$$\int_{S_e^{(j)}} f^*(\zeta_P,\zeta)N(\zeta)dA = \int_{S_e^{(j)}} \{f^*(\zeta_P,\zeta)N(\zeta)dA -$$

$$f^*(\zeta_P,\zeta')L_Q(\zeta')dA'\} +$$

$$\int_{S_e^{(J)}} f^*(\zeta_P, \zeta') L_Q(\zeta') dA' \tag{3.19}$$

where $f^*(\zeta_o, \zeta)$ and $f^*(\zeta_o, \zeta^P)$ represent either of the fundamental solutions evaluated on the element surface and on the tangent plane (respectively) and,

$$L_Q(\zeta) = N(\zeta_o) + \left.\frac{\partial N}{\partial \zeta_1}\right|_Q (\zeta'_1 - \zeta_1^Q) + \left.\frac{\partial N}{\partial \zeta_2}\right|_Q (\zeta'_2 - \zeta_2^Q). \tag{3.20}$$

When expressed in a specific local coordinate frame, the first derivatives in Equation (3.20) can be evaluated as simple functions of the mapping function derivatives and nodal point coordinates. Finally, semi-analytical integration of the regularizing terms is accomplished using the approach outlined above for fracture solutions in which each term of the fundamental solution is separated into radial and angular components.

Although this integration scheme permits evaluation of stress and displacement fields nearer to the element surface than previously possible, it is not generally the most cost-effective approach. For source points further from the element than the element dimension, straightforward two-dimensional numerical integration gives equivalent results and is less expensive [44].

The singular integrals associated with the boundary displacements need not be evaluated directly when considering finite, bounded regions. By virtue of a rigid body displacement, these terms can be equated to the sum of all other elemental integrals for the singular source point [51].

$$H_{II} = -\sum_{J \neq I} H_{IJ} \tag{3.21}$$

3.2.2 Boundary Conditions

In general three-dimensional elastostatics, three independent conditions must be specified at each boundary collocation point. These are typically the values of the

displacement and/or traction components in the global reference frame. However, several situations occur frequently which require special treatment, including Dirichlet corners, symmetric planes, and region interfaces (treated in Section 3.3 below).

The term 'Dirichlet corner' refers to a point along the model boundary at which the boundary tractions change discontinuously. In three-dimensions, any edge or corner can present modeling difficulties since more than two unknowns - the corner displacements and tractions for each neighboring face - must be handled with one equation system. The analogous situation in two-dimensions is depicted in Figure 3.2(a). For certain combinations of applied boundary conditions, the existing approach is sufficient. However, the problem becomes indeterminate when only the displacement components are prescribed.

Various approaches have been developed for this situation, including nodal point separation, discontinuous elements, and derivative formulations. In this implementation, distinct nodal points, separated by a small distance, are entered at such 'corners' to accommodate this difficulty. As shown in Figures 3.2(b) and 3.2(c), the distance between nodal points can either be spanned by a small element or left as a gap in the component boundary. Separation of the collocation points reduces the problem to determinate form by increasing the number of available equations. However, care must taken to separate the points sufficiently to create distinguishable equations and permit accurate integration, but not so far that the disruption of the component boundary affects the model. Typical values used for the matrix and fiber models range from 1/4 to 1/2 local element dimension.

Planes of symmetry, used to reduce and simplify models, can present similar difficulties. Boundary conditions along symmetric planes mandate that the normal displacement and tangential traction components be zero. When these planes are aligned with the reference axes, these conditions can be applied as prescribed boundary

displacements and tractions. However, for general planes of symmetry, the boundary relations become more complicated:

$$\mathbf{U}\cdot\mathbf{n}=\mathbf{0},$$

$$\mathbf{T}\cdot\mathbf{r}=\mathbf{0}, \quad \text{and} \quad \mathbf{T}\cdot\mathbf{s}=\mathbf{0} \tag{3.22}$$

$$\text{where } \mathbf{r}=\frac{\mathbf{r}_o-(\mathbf{n}\cdot\mathbf{r}_o)\mathbf{n}}{\left\|\mathbf{r}_o-(\mathbf{n}\cdot\mathbf{r}_o)\mathbf{n}\right\|} \quad \text{and} \quad \mathbf{s}=\mathbf{r}\times\mathbf{n}. \tag{3.23}$$

In Equation (3.23) $\mathbf{r}_o$ is some initial guess for the tangent vectors $\mathbf{r}$ and $\mathbf{s}$, and $\mathbf{n}$ is the outward unit normal. These additional equations are combined with the existing system of equations to relate the boundary values along symmetric planes so that the conditions

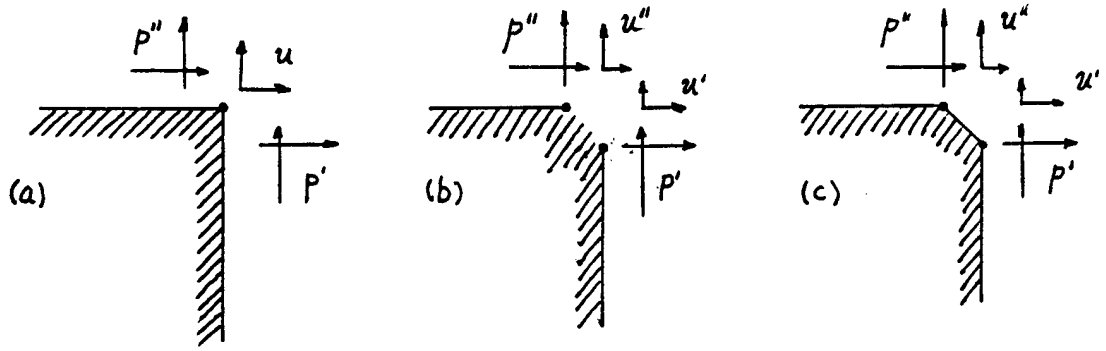

Figure 3.2 Treatment of Dirichlet Corners; Boundary points (a) at which discontinuities in the applied conditions create intractable problems (e.g. corners and edges subject to applied displacements) can be handled in the boundary element formulation by creating two distinct nodal points, joined (b) or unjoined (c), at the point of discontinuity. Separation of these nodes should be sufficient to distinguish the resulting equations and to permit accurate integration but should not disrupt the model. (Adapted from [51])

expressed in Equation (3.22) are prescribed in the solution.

To accurately simulate symmetric boundaries, corrective tractions applied to the boundary element model must reflect the variation in stress due to the proximal fracture elements. For reasons discussed later in this chapter, the local accuracy is dependent on the refinement of the boundary mesh, the relative surface integral/boundary element size and proximity of the crack elements to the boundary. To reduce computational errors for commonly used symmetry conditions, single-, two-, and three-fold symmetric crack elements are used for near-boundary fracture elements. These symmetries are incorporated in the surface integral technique by reflecting the fracture elements about the appropriate planes and condensing the resulting matrix terms. The effect in the hybrid method is to translate the influence of the fracture on the neighboring boundary from sharply-varying traction to milder displacement distributions. Because the evaluated terms are subject to computational noise, the condensed values must be filtered. Typical results are shown in Figures 3.5 and 3.6 for the case of a centrally located penny-shape fracture in a tensile bar. Even for low degree-of-freedom models, use of symmetric fracture elements reduces the errors in stress-intensity factors (and therefore crack-face displacements) for a wide range of relative element sizes.

3.3 Bimaterial Interface Models

An important aspect of the matrix crack model is the effect of interfacial slip and debonding. As described in Chapter 1, proper tailoring of the interfacial properties can be critical to the overall composite performance. A technique borrowed from contact mechanics analysis has been employed to provide a flexible means of incorporating this phenomenon in the SIBEH method.

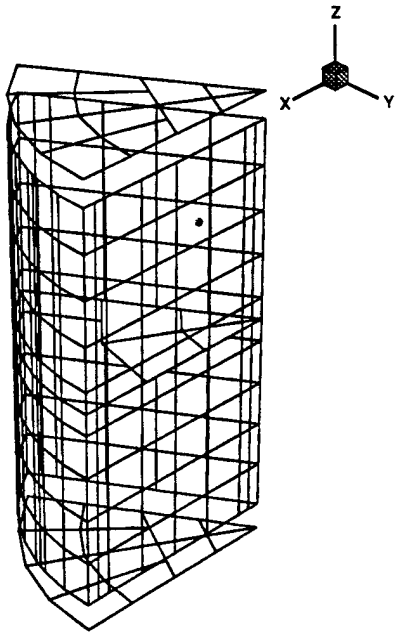

Figure 3.3 1/6 Symmetric Model of a Circular Crack in a Tensile Rod; The surface integral and boundary element meshes are shown for the 1/6 symmetric model used to evaluate the effectiveness of symmetric fracture elements.

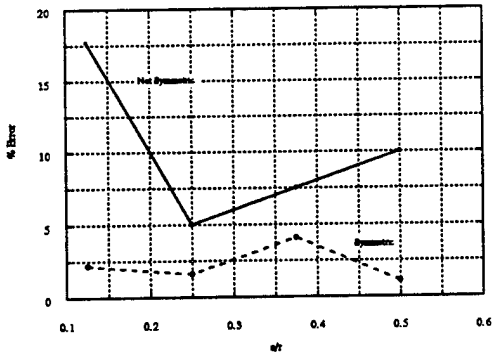

Figure 3.4 Symmetric Model Error Estimates; Error estimates for the 1/6 symmetric model shown in Figure 3.3 are plotted as a function of relative crack radius. In this model, the relative crack radius also represents the relative surface integral/ boundary element size, important for accurate fracture parameter solutions.

3.3.1 Interfacial Slip and Separation

The interfacial phenomenon relevant to composite damage mechanics can be modeled by three distinct situations: perfect bonding, interface debonding, and frictional slip. Bonding occurs during manufacture because of chemical interaction between the fiber and matrix or due to thermal strains acting across the interface and is modeled by enforcing displacement and traction continuity as described above. Interfacial debonding or slip are simulated by applying boundary tractions according to the composite microstructure and the local conditions. If the stresses acting normal to the interface are tensile and above a critical value, the interface debonds and the applied tractions become zero. This critical normal stress, σ_n, is used to reduce the effects of small numerical errors in interface tractions and can simulate the binding influence of thermal strains. The bonding/ debonding conditions are summarized in equation (3.24):

$$\begin{aligned} &\text{Bonding:} \quad \sigma \le \sigma_n \\ &\text{Debonding:} \quad \sigma > \sigma_n . \end{aligned} \tag{3.24}$$

Excessive shear in conjunction with sub-critical normal stresses leads to interfacial slip, which may be simulated in one of two manners. A Coulombic friction rule is commonly used, in which the interfacial shear stress is proportional to the local normal stress (according to friction coefficient, μ) and is taken in the direction opposite impending slip:

$$\tau = \begin{cases} \tau & \text{for} \quad \tau < \mu|\sigma| \quad \text{and} \quad \sigma \le \sigma_n \\ \mu|\sigma| & \text{for} \quad \tau < \mu|\sigma| \quad \text{and} \quad \sigma \le \sigma_n \end{cases} . \tag{3.25}$$

Interfacial sliding on this scale for fiber-matrices is small so that it may be appropriate to use the static or break-away friction coefficient rather than the kinetic coefficient. These values are determined from fiber push-out or pull-out tests [32-34].

An alternative interface model is constant shear stress, in which the critical sliding stress, τ_{CRIT}, is a constant model parameter:

$$\tau = \tau_{CRIT} \quad \text{for} \quad \tau < \tau_{CRIT} \quad \text{and} \quad \sigma \leq \sigma_n. \tag{3.26}$$

As in the Coulomb friction model, the sliding shear stress acts in a direction opposite slip. This model is a simpler approximation and is sufficient for many ceramic composite systems, including SiC/LAS [34].

Although the iterations required for convergence may differ, the approach to solving the non-linear interface problem is the same for both interface models. The simplest approach is to completely solve the non-linear interfacial slip problem for each crack advance. For each fracture configuration, the interfacial nodes are sampled and updated according to the criteria expressed in Equation (3.25) or (3.26) until convergence. For crack propagation problems, the interfacial slip zone is recorded and used as an initial condition for subsequent fracture geometries. This reduces the number of iterations required for small fracture steps, and improves the converged solution.

Even with special matrix solvers, this process is costly. Improvements in the non-linear solution strategy can lead to large reductions in computational effort. Although it has not been implemented here, Larson successfully employed an iterative scheme which estimated fracture advance and interfacial slip alternately [26]. Further numerical issues which have been addressed include interpenetration of opposing faces and low-level oscillations in the normal stress.

3.3.2 Experimental Verification

For sufficiently weak interfaces, interfacial slip actually occurs ahead of the fracture tip [2,26]. In fact, this debonding is critical to reduction of fiber stresses for toughened failure behavior. To verify the accuracy of the interfacial model employed, an

interface slip zone has been generated and observed using the Interface Slip Experiment apparatus developed by Larson and rebuilt for this investigation [26]. Experimental results serve as a qualitative indicator of the slip zones expected on curved fiber-matrix interfaces and give a quantitative assessment of the computational simulations.

The experimental apparatus depicted in Figure 3.5 consists of a Sylastic rubber block constrained between two 'rigid' PMMA plates. A penny-shaped flaw approaching the interface is simulated with an inflatable rubber diaphragm located beneath the rubber block. The interface conditions can be varied by changing the confining strains (measured with strain gages) and the interfacial coating. Although the rubber material does not behave like a brittle ceramic, its use allows interfacial deformations to be observed directly by comparing grids marked on both the block and on the PMMA.

Figure 3.6 shows a typical experimental slip pattern and the slip zone predicted using the 1/4 symmetric model shown in Figure 3.7. For this case, the interface slip model is defined by a constant shear stress estimated by Larson [26]. Both the predicted slip zone location and the relative displacements show good agreement with experimental results. Although there is a slight difference in the extent of the slip zone, the effect of this on a neighboring fracture is expected to be relatively small.

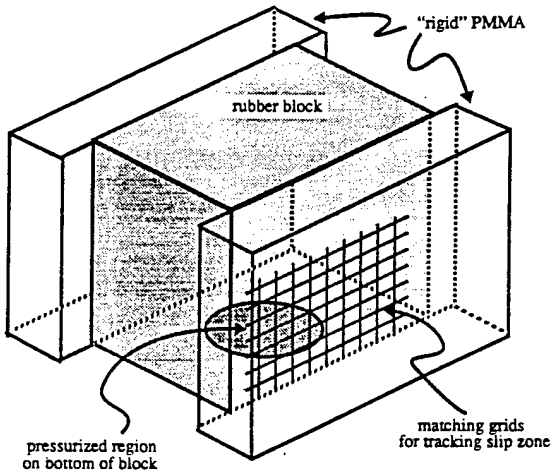

Figure 3.5 Interface Slip Experiment; This experimental apparatus generates observable frictional interface slip ahead of an internally pressurized penny-shaped crack. Both the interface conditions and the confining normal strains can be varied (From [26])

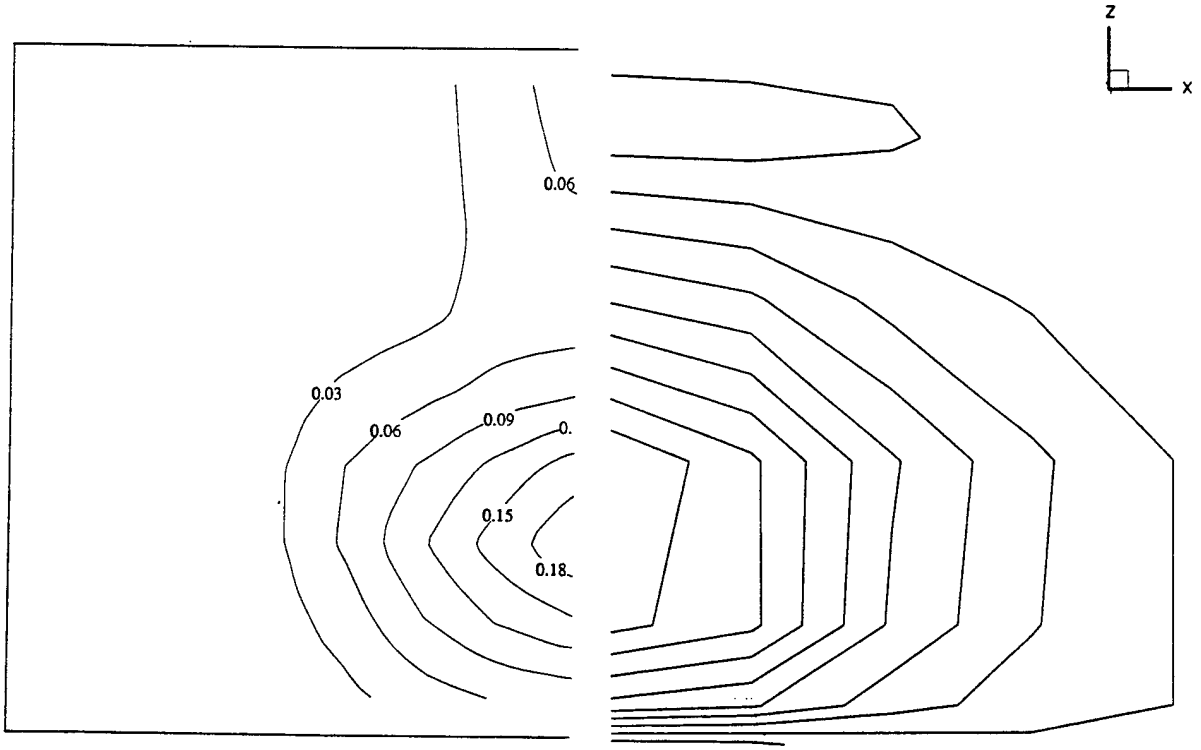

Figure 3.6 Experimental and Computational Interface Slip; Predicted slip along a planar bimaterial interface show good agreement in general shape, location, and magnitude with experimental slip zones observed using the Interface Slip Experiment [26].

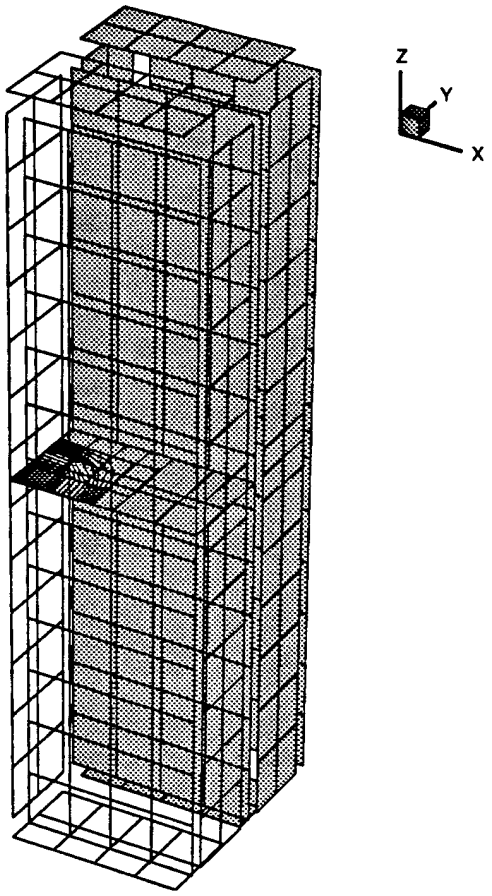

Figure 3.7 1/4 Symmetric Model of Interface Slip Experiment; Surface integral and boundary element subregion meshes are shown for a 1/4 symmetric model of the Interface Slip Experiment. A contour plot of interfacial slip has been superimposed.

3.4 Numerical Issues

Several numerical issues have arisen during this investigation regarding the accuracy of the hybrid method solutions and are discussed briefly here.

3.4.1 Solution Accuracy

Investigations of the error sources in the SIBEH method for situations pertinent to fracture growth in composite media indicate that the fracture parameter solutions are most

sensitive to the collocation distribution (fracture and boundary meshes) and - to a lesser extent - the integration order. Attempts at iterative improvement of the solution resulted in insignificant changes, indicating that the solution scheme (LU decomposition with partial pivoting) performs well, even for large problems (>5000 degrees of freedom).

This initial investigation has developed and made use of several meshing heuristics to improve solution accuracy. These guidelines can easily be incorporated in mesh generators, although they have not yet been implemented in this fashion. Although some flexibility can be tolerated, best results are obtained with uniform collocation point density. For fracture models, this means relative element sizes proportional to the number of collocation points per element as discussed in Chapter 2. Most commonly, crack-tip elements should be roughly twice as large as neighboring constant elements. Use of Lagrange family elements and uniform mesh densities have addressed this issue for the boundary element models. Other common error sources include severely distorted elements and small corner angles [45,51].

Additional issues arise with the combination of the surface integral and boundary element methods. The fracture surface must be sufficiently refined to accurately model the crack-opening displacements. The boundary element mesh should reflect local boundary value variations due to the presence of the crack and the applied conditions. However, the integration errors for both techniques increase with relative source point proximity (See Figure 3.4 above). While some special conditions can be simulated directly (e.g. symmetric fracture elements), these conflicting demands must generally be balanced.

3.4.2 Improved Iterative Scheme

The presence of a significant number of zero terms in the multi-region equation system described by Equation (3.17) suggests opportunities for improved storage and

solution schemes [60,61]. For this investigation, an iterative improvement scheme has been developed which achieves these goals. The technique applies interfacial traction condition only to the larger fracture-matrix model so that this equation system can be decomposed and stored. Separate systems of equations are setup and decomposed for additional subregions (e.g. fibers) for each interface-slip step. Bonded interface points in the fiber models are subject to the corresponding matrix displacements. The routine iterates between the models in this fashion until convergence to guarantee satisfaction of the interface continuity (See Figure 3.10).

For the cracked matrix model at solution iteration j:

$$\begin{bmatrix} C-DJ+SL & S^1 & S^{INT} \\ GJ-HL & H^1 & H^{INT} \end{bmatrix} \begin{Bmatrix} \delta \\ U^1 \\ U^{INT} \end{Bmatrix}_{j+1} = \begin{Bmatrix} t+D^1T^1 \\ G^1T^1 \end{Bmatrix} + \begin{bmatrix} D^{INT} \\ G^{INT} \end{bmatrix} \{T^{INT}\}_j \qquad (3.27)$$

The initial interface traction conditions are taken from the previous fracture analysis in crack-growth studies to reduce number of iterations required for convergence.

The corresponding relations for the attached fiber regions can be expressed in matrix form as:

$$\begin{bmatrix} H^2 & -G^{INT} \end{bmatrix} \begin{Bmatrix} U^2 \\ T^{INT} \end{Bmatrix}_{j+1} = \{G^2T^2\} + [-H^{INT}]\{U^{INT}\}_j \qquad (3.28)$$

The iterative scheme is effective since the boundary conditions imposed on the matrix interface points do not change type when slip occurs. This removes a decomposition of the main equation system (N^3 operation) from the interface slip loop, leaving only the substitution required for each solution step (N^2 operations). For typical matrix crack model sizes, this approach results in a reduction of effort when less than 200 iterations are required for convergence. It is important to note that this is not generally true. For

systems with stiffer fibers, the interfacial tractions must be damped to guarantee convergence. The best approach depends on the model geometry and material properties.

3.4.3 Computational Efficiency

One goal of this research program has been to develop a computational fracture mechanics scheme which can be operated on mid-range computers. While the SIBEH code developed for the matrix crack analyses has been tested and run on CRAY supercomputers, the results presented in this document were generated on a DEC-Station 3100. Large degree-of-freedom problems have been solved in several hours with the use of symmetric condensations, semi-analytic integration schemes, and the iterative multi-region solution scheme described above. Since most of the computational effort involves integration, storage of the model equation systems in formatted, direct-access files significantly reduces the time required for repeated analyses of the same model subject to different boundary or interface conditions [62].

Chapter 4

Small Matrix Crack Growth in Ceramic Composite Materials

The application of the computational approach developed in Chapters 2 and 3 to matrix crack initiation and subsequent propagation is presented in this chapter. Results for a fully three-dimensional analysis of small crack growth in a silicon carbide fiber-reinforced glass-ceramic subject to remote tensile stresses are outlined with particular attention to matrix cracking stresses and fiber failure. A discussion of findings and their relation to other matrix crack theories is included as well. The implications for toughened ceramic materials are discussed in Chapter 5.

4.1 Small Matrix Crack Models

The composite system modeled in this investigation consists of a glass-ceramic matrix reinforced by 40% volume silicon carbide fibers aligned with the loading direction as depicted in Figure 4.1. The constituent material properties and microstructural conditions are summarized in Table 4.1. The interface is modeled with no thickness and is governed by constant shear stress conditions as suggested for this material combination by experimental results. Four interfacial strengths will be evaluated, ranging from lightly bonded (2 MPa) to strongly bonded (40 MPa).

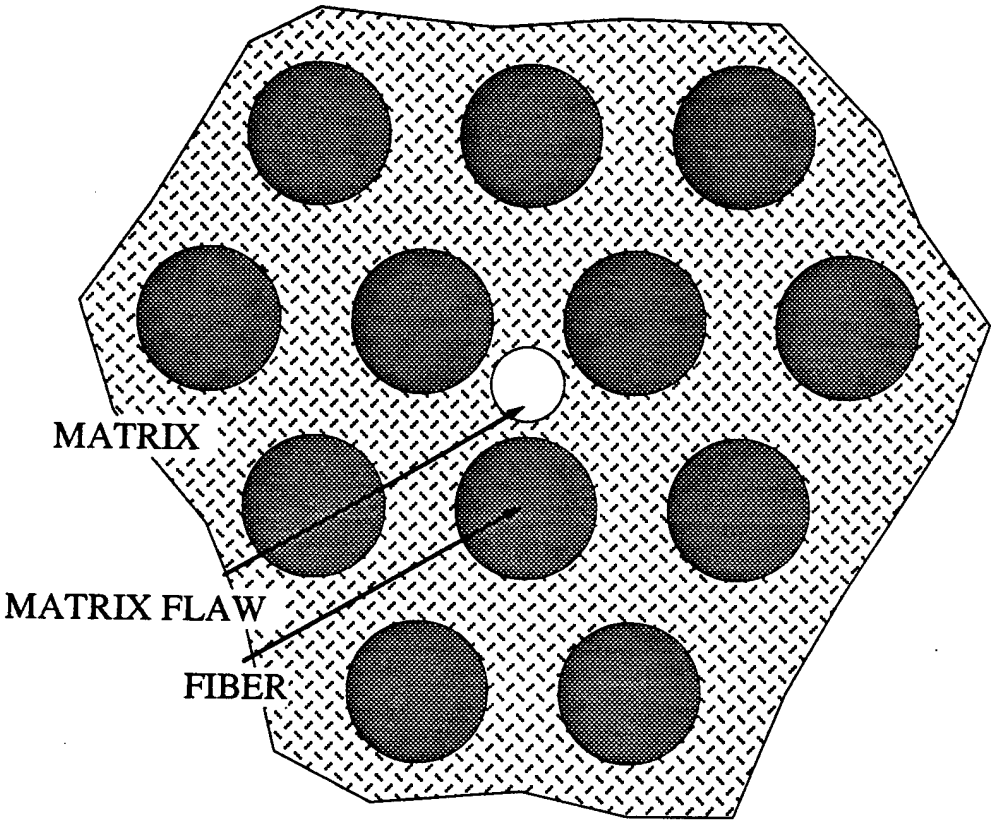

Figure 4.1 Matrix Crack Initiation Configuration; The matrix crack model simulates an initially circular flaw propagating in a glass-ceramic matrix stiffened by hexagonally-packed silicon carbide fibers. This particular configuration is based on experimental observations for this material system [4,5].

The matrix crack is assumed to begin as a penny-shaped flaw located between the fibers and aligned perpendicular to the fiber and loading direction. This configuration is based on acoustical and optical observations of crack initiation in this particular material system and has been modeled using approximate methods to determine the matrix cracking stress [4,5,19,27]. The model constructed for this situation describes matrix crack intiation and subsequent growth when the fracture is on the order of the fiber spacing. The scope has been chosen to bridge the gap from the initiation point to the axisymmetric models of 'intermediate' size (i.e. several fiber spacings in size, but less

Table 4.1 SiC/LAS Composite Material Properties; [7,15]

SiC fiber:	E_f	200 GPa
	ν_f	0.2
	S	2 GPa at room temp. 1 GPa at 1000 C
	R	8 μm
LAS matrix:	E_m	85 GPa
	ν_m	0.3
	K_{IC}^m	2 MPa$\sqrt{m}$
	γ_m	21 J/m^2
Composite:	V_f	0.40
	τ	2 - 40 MPa

than critical transition flaw size) [18]. The model is further reduced using symmetric boundary conditions and condensation to include the regions depicted in Figure 4.2.

4.1.1 Matrix Crack Initiation

The primary focus of this investigation is the behavior of matrix cracks initiating between fibers and propagating past the first rows of fibers. The 1/6 symmetric model incorporates the stiffening effects of the first two fibers and has been tested for three distinct crack lengths subject to four interface conditions. The mesh and model cell are shown in Figure 4.3. The model consists of roughly 2500 degrees of freedom (including coincident interface points) before condensation for vertical symmetries and requires slightly more than 2 hours for complete interface slip analysis.

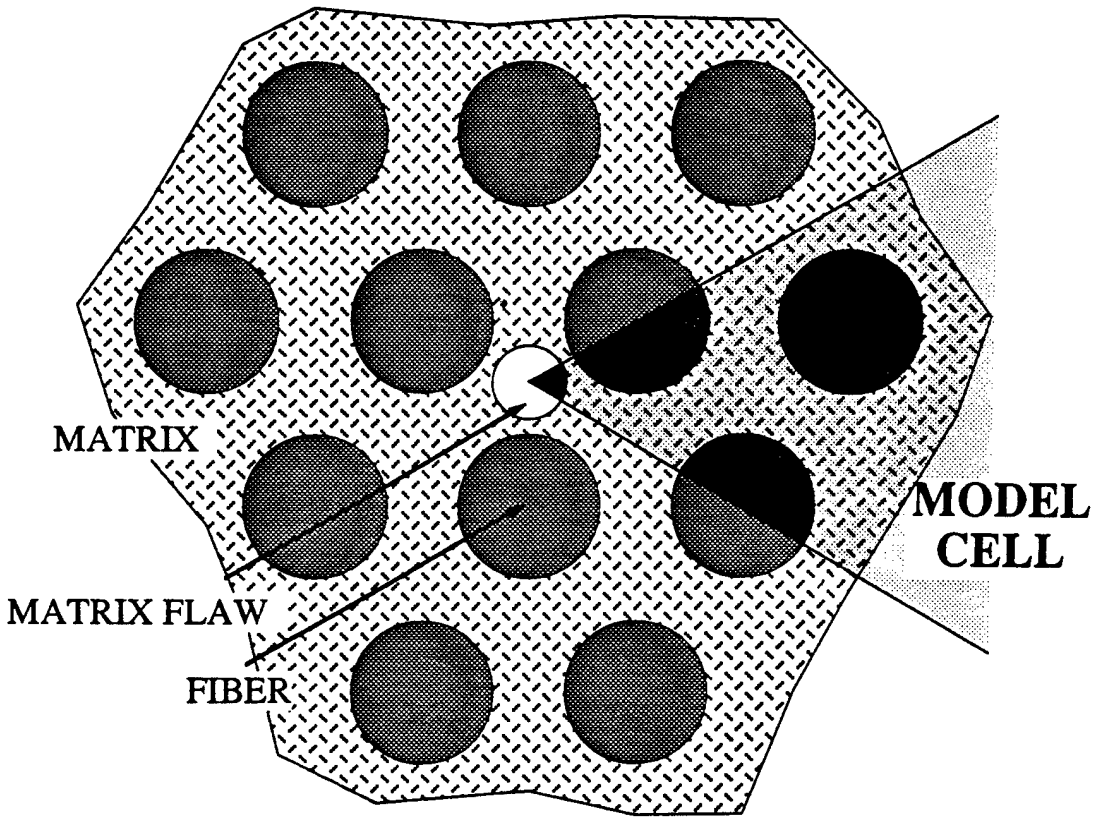

Figure 4.2 Small Matrix Crack Configuration and Model Cell; Model cell boundaries are constructed using symmetry as shown for investigation of matrix crack initiation and subsequent small matrix crack growth.

To simulate remote applied strains, the upper and lower surfaces are constrained. More accurate results are obtained for pressurized fractures than for remote loading, so the actual boundary conditions imposed include zero displacements on the upper and lower surfaces, internal pressure on the fracture surface ($p=E_m\varepsilon$), and the appropriate symmetric and interfacial boundary conditions. The superposed solutions are equivalent for the constant shear stress interface model. Stress intensity factors, remote loads, and fiber stresses have been computed for three distinct crack configurations (See Figure 4.4) subject to a range of interfacial strengths, including 2 MPa, 20 MPa, and 40 MPa. This range was chosen to include both brittle and toughened failure modes and to coincide with experimental data. Results of these analyses are presented below in Section 4.2.

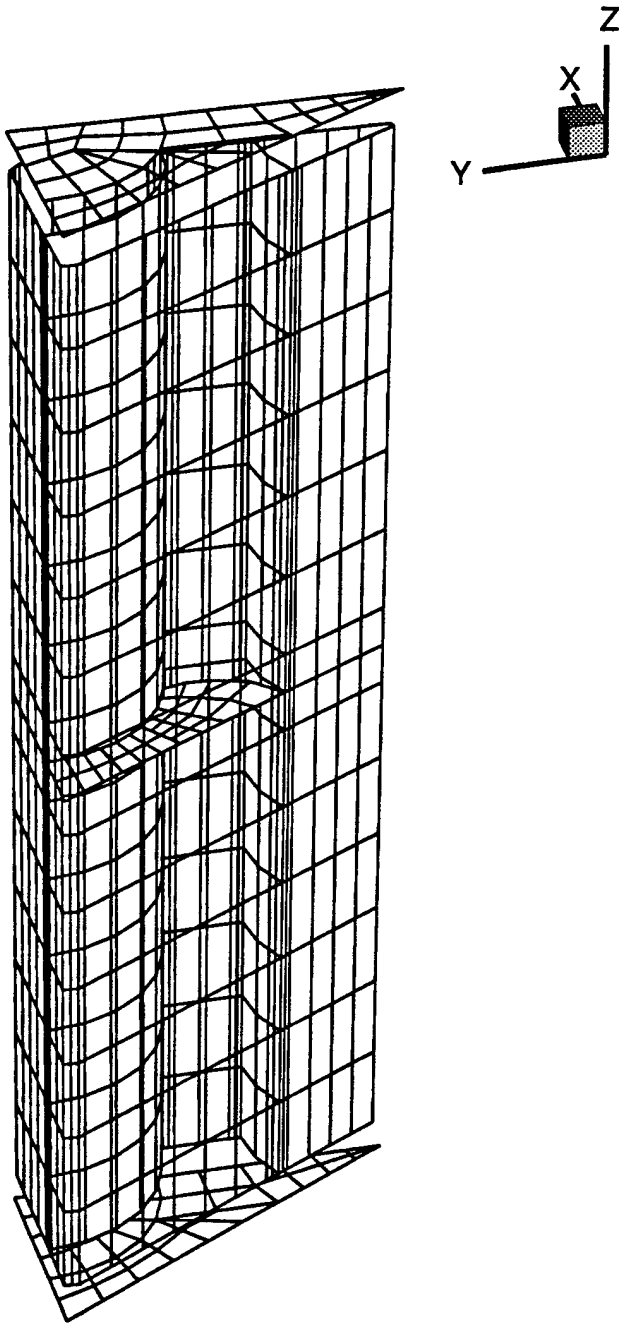

Figure 4.3 Matrix Crack Initiation Model; Matrix, fiber and fracture discretization is shown for the matrix crack intitiation model constructed for analysis of matrix crack initiation subject to varying interfacial shear stress (2-40 MPa). The complete model consists of roughly 2500 degrees of freedom.

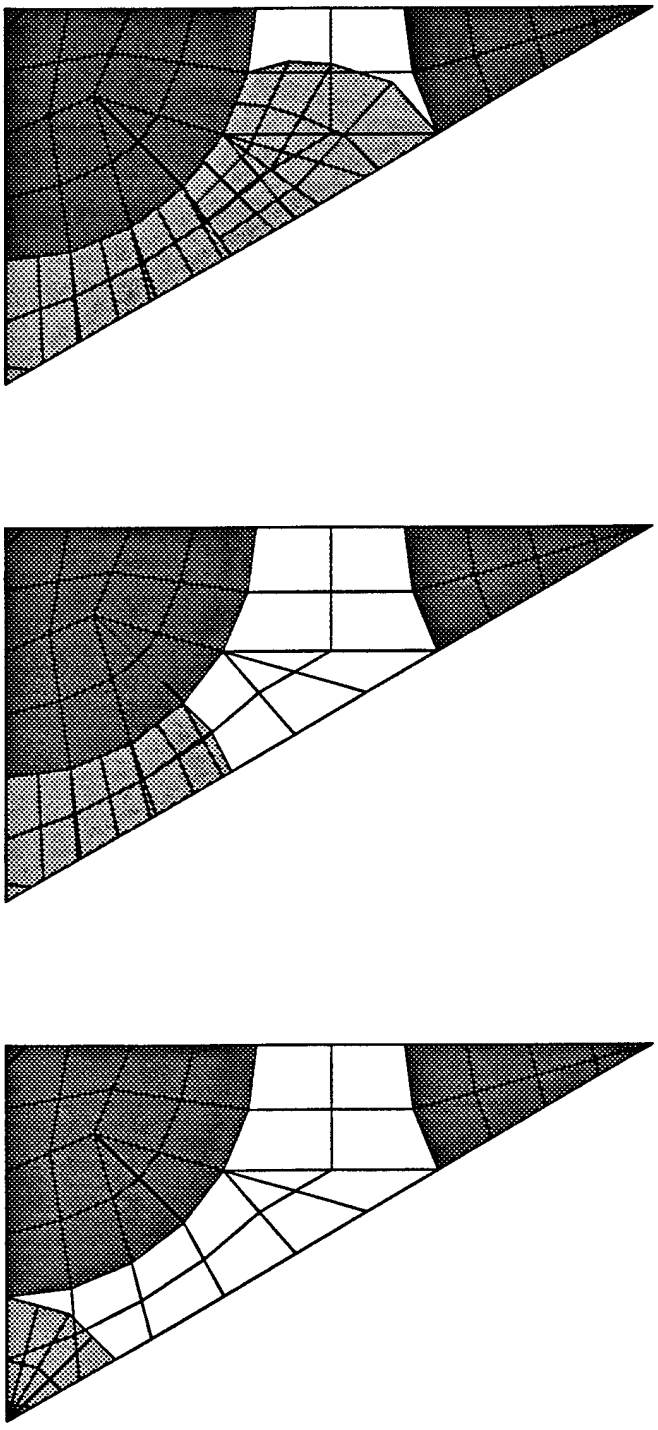

Figure 4.4 Matrix Crack Configurations; Three matrix crack fronts and surface integral meshes are shown for analysis of small crack growth subject to the stiffeneing effects of the first two fibers.

4.2 Fracture Parameter Results

4.2.1 Matrix Cracking Stress

The estimated matrix cracking stresses for both models are plotted in normalized form in Figure 4.5 and tabulated as effective toughness in Table 4.2.

Table 4.2 Effective Toughness for Small Crack Propagation;

K_{eff}/K_{IC}			
c/R \ τ	2 MPa	20 MPa	40 MPa
0.5	5.95	6.90	7.30
1.0	5.80	6.76	7.19
2.0	5.42	6.27	7.09

4.2.2 Fiber Stresses

Because the toughenig mechanisms and notch insensitivity of fiber-reinforced ceramics rely on the presence of fracture-bridging fibers, the isolation of the fibers from crack-tip stresses is critical to successful use of these materials in structural applications. The axial fiber stresses are estimated as a function of the shape function derivatives and the collocation point displacements and computed for each of the modeled fibers. Typical stress contours are shown in Figure 4.6 for the matrix crack initiation model and the maximum is plotted as a function of characteristic crack length for the interfacial conditions considered (See Figure 4.7).

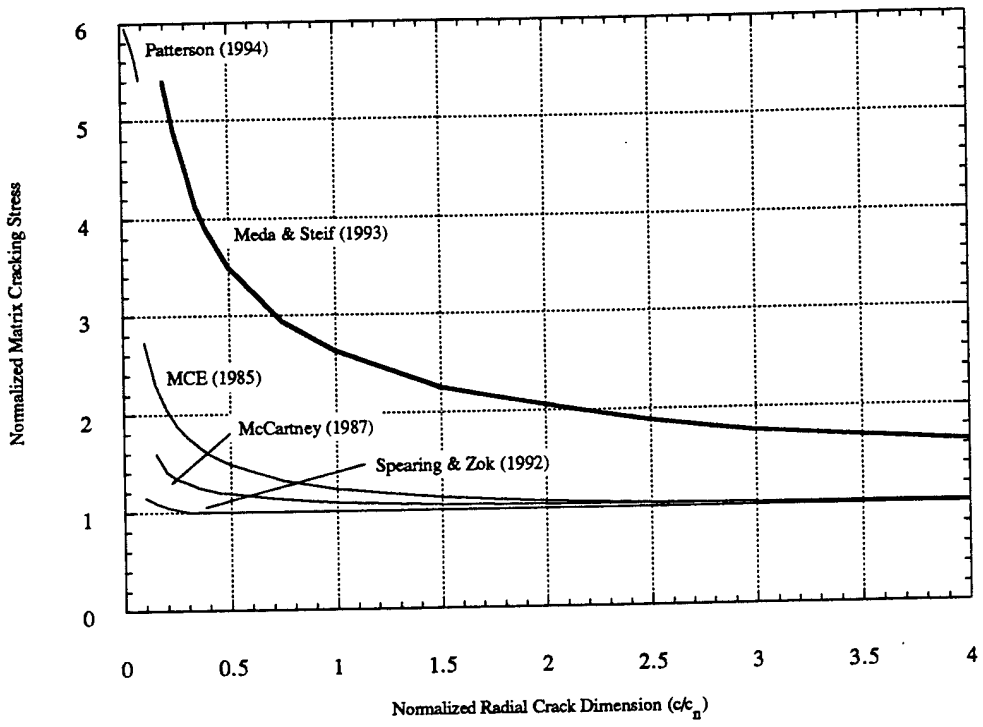

Figure 4.5 Matrix Cracking Stress for Small Cracks; Normalized values for the matrix cracking stress are plotted along with 'intermediate' crack solutions.

4.3 Discussion of Results

Recent results derived by Meda and Steif suggest that steady-state matrix cracking may occur in ceramic composite materials, a posssibility that holds great promise for structural engineers. The results of this investigation support the steady-crack hypothesis and appear to be consistent with these 'intermediate' crack length models (See Figure 4.5). In particular, the effective toughening due to crack pinning and interfacial slip have been shown to be significantly higher than previous estimates. Furthermore, the effective toughness prior to fiber failure is dependent on the interfacial shear for small crack growth. This is an anticipated result of the crack pinning in a region of interfacial sliding

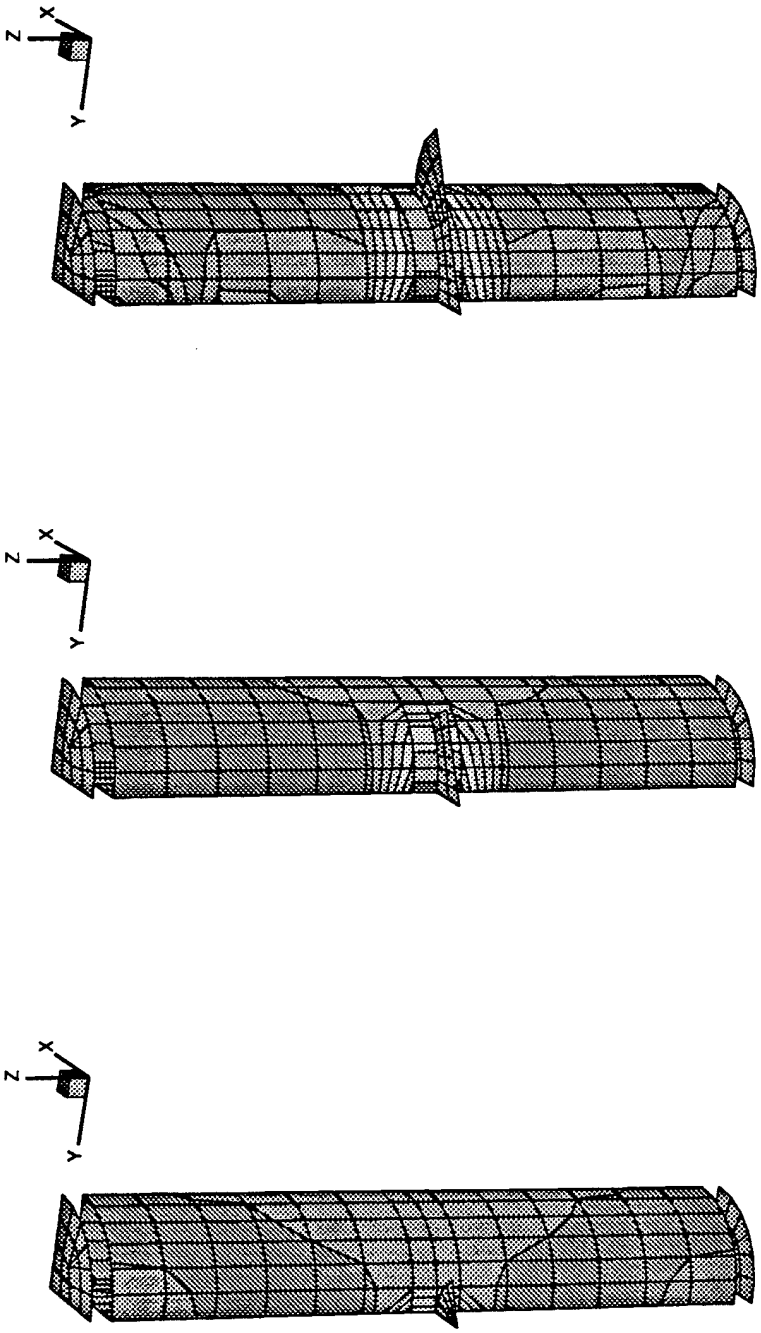

Figure 4.6 Fiber Stress Contour Plots; Fiber stress contours are shown for the first fiber with string interfacial bonding (40 MPa).

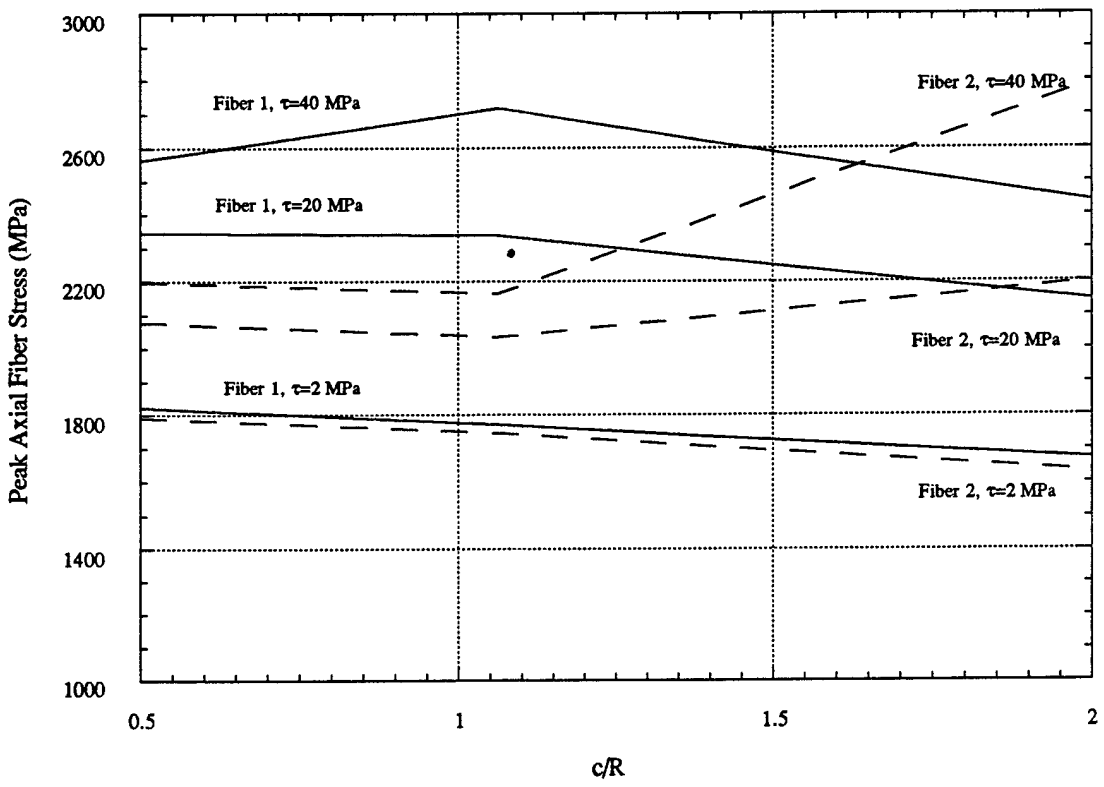

Figure 4.7 Peak Axial Fiber Stress for Proximal Fibers; The peak axial fiber stress due to small matrix crack extension is plotted for proximal fibers.

and of the relative scale of the fracture.

These results show that failure of the first or second fiber (depending on the load transfer and interface slip) can occur in the presence of small matrix flaws. Relatively low interfacial strengths are required to safely isolate the fibers from the crack-tip stresses. For the SiC/LAS system modeled, interface sliding stresses slightly above 2 MPa can lead to failure at room temperature. This is consistent with experimental evidence and may have serious implications for composites reinforced with embrittled fibers with degraded strengths [7]. General ceramic composite systems are expected to demonstrate similar behavior.

Chapter 5

Conclusions and Recommendations

5.1 Conclusions

A matrix crack model has been constructed for small crack growth based on experimental observations of crack location and matrix cracking stress in silicon carbide reinforced lithium alumino-silicate (SiC/LAS) [4,5]. Kim and Pagano have observed matrix crack initiation in the region between the reinforcing fibers and on the scale of the fiber spacing [4]. More importantly, this initial fracture propagation occurs prior to observable non-linearities in the composite load-deflection relationship which signify either brittle failure or toughened fracture.

This situation has been analyzed in conjunction with interface slip using numerical techniques and more recently using an axisymmetric distributed spring model [18,27]. This improved axisymmetric model suggests the possibility of stable fracture growth for small crack sizes and weak interfacial conditions. Stable matrix crack propagation is a possibility not previously considered feasible but with significant implications for the design of toughened ceramic materials.

The results of this investigation support the steady-crack hypothesis and are consistent with 'intermediate' crack length models (See Figure 4.5). In particular, the effective toughening due to crack pinning and interfacial slip have been shown to be significantly higher than previous estimates. Small fractures propagating among

reinforcing fibers are shielded from the applied loads as expected. Though it is difficult to confirm with the data collected to date, the three-dimensional nature of composites on this scale appears to be important and slows the decrease in matrix cracking stress as the fracture propagates. Despite this temporary change, the magnitudes of the critical stress are close to those derived by Meda and Steif using the axisymmetric model [27].

The propagation behavior of small matrix flaws is critical to the toughening mechanisms available for large fractures and is dependent on the interfacial strength. As shown in Figure 4.7, failure of the first or second fiber (depending on the load transfer and interface slip) can occur at relatively low interfacial strengths. For the SiC/LAS system modeled, interface sliding stresses above 12 MPa can lead to failure at room temperature and guarantee failure of degraded fibers [7]. General ceramic composite systems are expected to demonstrate similar behavior.

On a different level, this investigation has developed and demonstrated an efficient computational technique for analysis of three-dimensional fracture growth in composite media. The technique appears to be particularly well-suited for microstructural models such as the matrix crack model analyzed in this investigation and ready for extension to thermo-elastic fatigue.

5.2 Recommendations for Further Work

While this research project has resolved some issues regarding matrix crack initiation in fiber-reinforced ceramics, it leaves many issues unresolved - by the nature of it finite scope - and poses as many more. Some of these issues are mentioned briefly here with the hope that continued research may soon resolve them.

The results presented are for a single crack propagating from a small matrix flaw. While it is possible that a large, 'steady-state' crack can form by extension of a single flaw

, it is more likely to be form by coalescence of many small flaws. The interaction between neighboring flaws is an important concept to the overall behavior of the material. In addition, the link between these microscopic material events and the macrostructural behavior of the material is critical to the successful development of these materials.

Equally important are the implications this damage development process may have on useful service life and maintenance. Toughened materials which can be tested in-service during regular maintenance intervals will find greater use and be more reliable. Proper tailoring of the interface offers some opportunities in this direction.

Many issues regarding chemical interaction and environmental evolution of the constituent have only recently been addressed. While it is now possible to tailor interfaces to provide toughened material behavior and failure modes, the same materials suffer structural failure at high temperatures and in corrosive environments [7]. Extension to harsher environments (e.g. irradiation) presents further complications.

Despite these unresolved issues, continued interest in the development and analysis of these materials combined with efforts for the economical manufacture of constituent materials promises bright futures for the use of ceramics for high-temperature structural applications

References

[1] Prewo, Karl M. 1988. Glass and Ceramic Matrix Composites: Present and Future. In *Material Research Society Symposium Proceedings Vol. 120*, 145-156.

[2] Evans, Anthony G. 1990. Perspectives on the Development of High-Toughness Ceramics. *J. Am. Ceram. Soc.*, 73[2]: 187-206.

[3] Davidge, R.W. 1989. The Mechanical Properties and Fracture behaviour of Ceramic-Matrix Composites (CMC) Reinforced with Continuous Fibres. In *Applications of Fracture Mechanics to Composite Materials*, ed. K. Friedrich, 547-569.

[4] Kim, R.Y. and N.J. Pagano. 1988. Initiation of Damage in Unidirectional Brittle Matrix Composites. In *Proc. Fourth USA-Japan Conf. Composite Materials*, 799-812, Lancaster, PA: Technomic, 1988.

[5] Barsoum, M.W., P. Kangutkar, and A.S.D. Wang. 1992. Matrix Crack Initiation in Ceramic Matrix Composites Part I: Experiments and Test Results. *Composites Science and Technology*, 44: 257-269.

[6] Marshall, D.B. and A.G. Evans. 1985. Failure Mechanisms in Ceramic-Fiber/ Ceramic-Matrix Composites. *J. Am. Ceram. Soc.*, 68[5]: 225-231.

[7] Luh, E.L. and A.G. Evans. 1987. High-Temperature Mechanical Properties of a Ceramic Matrix Composite. *J. Am. Ceram. Soc.*, 70[7]: 466-469.

[8] Bower, A.F. and M. Ortiz. 1991. A Three-Dimensional Analysis of Crack Trapping and Bridging by Tough Particles. *Journal of Mechanics and Physics of Solids*, 39[6]: 815-858.

[9] He, M.Y. and J.W. Hutchinson. 1988. Crack Deflection at an Interface between Dissimilar Elastic Materials. Report MECH-133, Division of Applied Sciences, Harvard University.

[10] Xu, Guanshui. 1994. Three Dimensional Elastic Analysis of Crack Growth and Toughening Mechanisms of Brittle Matrix Composites. Ph.D. diss., Brown University.

[11] Aveston, J. and A. Kelly. 1973. Theory of Multiple Fracture of Fibrous Composites. *J. Mat. Science*, 8:352-362.

[12] Aveston, J., G.A. Cooper, and A. Kelly. 1971. Single and Multiple Fracture. In *The Properties of Fiber Composites*, 15-26, National Physical Laboratory, Guilford, UK. IPC Science and Technology Press.

[13] Budiansky, B. and J.W. Hutchinson. 1986. Matrix Fracture in Fiber-Reinforced Ceramics. *J. Mechs. Phys. Solids*, 34[2]: 167-189.

[14] Marshall, D.B. and B.N. Cox. 1987. Tensile Fracture of Brittle Matrix Composites: Influence of Fiber Strength. *Acta. Metall.*, 35[11]: 2607-2619.

[15] Marshall, D.B., B.N. Cox, and A.G. Evans. 1985. The Mechanics of Matrix Cracking in Brittle-Matrix Fiber Composites. *Acta. Metall.*, 33[11]: 2013-2021.

[16] McCartney, L.N. 1987. Mechanics of Matrix Cracking in Brittle-Matrix Fibre-Reinforced Composites. *Proc. R. Soc. London A*, 409:329-350.

[17] McMeeking, R.M. and A.G. Evans. 1990. Matrix Fatigue Cracking in Fiber Composites. *Mechanics of Materials*, 9:217-227.

[18] Meda, G. and P.S. Steif. 1993. A Detailed Analysis of Cracks Bridged by Fibers Part I: Limiting Cases of Short and Long Cracks. Report SM 93-5, Dept. of Mechanical Engineering, Carnegie Mellon University.

[19] Meda, G. and P.S. Steif. 1993. A Detailed Analysis of Cracks Bridged by Fibers Part II: Cracks of Intermediate Size. Report SM 93-6, Dept. of Mechanical Engineering, Carnegie Mellon University.

[20] Cook, J. and J.E. Gordon. 1964. A Mechanism for the Control of Crack propagation in All-Brittle Systems. *Proc. R. Soc. London A*, 282:508-520.

[21] Evans, A.G. 1972. The Strength of Brittle Materials Containing Second Phase Dispersions. *Phil. Mag.*, 26: 1327-1344.

[22] Lange, F.F. 1971. Fracture Energy and Strength Behavior of a Sodium Borosilicate Glass-Al_2O_3 Composite System. *J. Am. Ceram. Soc.*, 54[12]: 614-620.

[23] Rose, L.R.F. 1987. Toughening Due to Crack-Front Interaction with a Second-Phase Dispersion. *Mechanics of Materials*, 6:11-15.

[24] Fares, N. 1988. Crack Fronts Trapped by Arrays of Obstacles: Numerical Solutions Based on Surface Integral Representation. Report MECH-136, Division of Applied Sciences, Harvard University.

[25] Gao, H. and J.R. Rice. 1989. A First-Order Perturbation Analysis of Crack Trapping by Arrays of Obstacles. *J. Applied Mechs.*, 56: 828-836.

[26] Larson, Michael C. 1992. Theoretical and Experimental Analysis of Toughening in Brittle Matrix- Brittle Fiber Ceramic Composites with Frictional Interfaces. Ph.D. diss., Massachusetts Institute of Technology.

[27] Wang, A.S.D., X.G. Huang, and M.W. Barsoum. 1992. Matrix Crack Initiation in Ceramic Matrix Composites Part II: Models and Simulation Results. *Composites Science and Technology*, 44:271-282.

[28] Mower, Todd M. 1993. Experimental Investigations of Crack-Trapping in Brittle Heterogeneous Solids. Ph.D. diss., Massachusetts Institute of Technology.

[29] Spearing, S.M. and F.W. Zok. 1992. Stochastic Aspects of Matrix Cracking in Brittle Matrix Composites. Internal Report, Materials Department, University of California, Santa Barbara.

[30] Cleary, M.P. 1977. Fundamental Solutions for a Fluid-Saturated Porous Solid. *Int. J. Solids Structures*. 13: 785-806.

[31] Kingery, W.D., H.K. Bowen, and D.R. Uhlmann. 1976. *Introduction to Ceramics*. New York: John Wiley & Sons.

[32] Liang, C. and J.W. Hutchinson. 1993. Mechanics of the Fiber Pushout Test. *Mechanics of Materials*, 14: 207-221.

[33] Marshall, D.B. and W.C. Olivier. 1987. Measurement of Interfacial Mechanical Properties in Fiber-Reinforced Ceramic Composites. *J. Am. Ceram. Soc.*, 70[8]: 542-548.

[34] Weihs, T.P. and W.D. Nix. 1991. Experimental Examination of the Push-Down Technique for Measuring the Sliding Resistance of Silicon Carbide Fibers in a Ceramic Matrix. *J. Am. Ceram. Soc.*, 74[3]:524-534.

[35] Keat, William D. 1989. Surface Integral and Finite Element Method for the Analysis of Three-Dimensional Fractures. Ph.D. diss., Massachusetts Institute of Technology.

[36] Cruse, T.A. 1988. *Boundary Element Analysis in Computational Fracture Mechanics*. Boston: Kluwer Academic Publishers.

[37] Annigeri, Balkrishna S. 1984. Surface Integral Finite Element Hybrid Method for Localized Problems in Continuum Mechanics. Sc.D. diss., Massachusetts Institute of Technology.

[38] Annigeri, B.S. and M.P. Cleary. 1982. Surface Integral Finite Element Hybrid (SIFEH) Method for Fracture Mechanics. Report REL-82-21, Massachusetts Institute of Technology.

[39] Bsaibes, Riad J. 1991. Analysis of Three-Dimensional Fractures Subject to Thermal Loading. B.S. thesis, Massachusetts Institute of Technology.

[40] Keat, W.D., B.S. Annigeri, and M.P. Cleary. 1988. Surface Integral and Finite Element Hybrid Method for Two- and Three-Dimensional Fracture Mechanics Analysis. *Int. J. Fracture*. 36: 35-53.

[41] Lam, K.Y. 1984. The Development of a Fully Three-Dimensional Simulator for Analysis of Three-Dimensional Fractures. Ph.D. diss., Massachusetts Institute of Technology.

[42] Narendran, Vasantha M. 1986. Analysis of the Growth and Interaction of Multiple Plane Hydraulic Fractures. Sc.D. diss., Massachusetts Institute of Technology.

[43] Rongved, L. 1955. Force Interior to One of Two Joined Semi-Infinite Solids. In *Second Midwestern Conference on Solid Mechanics* held in Lafayette, IN.

[44] Cruse, T.A. and R. Aithal. 1993. Non-Singular Boundary Integral Equation Implementation. *Int. J. for Num. Methods in Engin.*, 36:237-254.

[45] Zienkiewicz, O.C. and R.L. Taylor. 1989. *The Finite Element Method.* Vol. 1. 4th ed. New York: McGraw-Hill Book Company.

[46] Portela, A., M.H. Aliabadi, and D.P. Rooke. 1993. Dual Boundary Element Analysis of Fatigue Crack Growth. In *Advances in Boundary Element Methods for Fracture Mechanics*, eds. M.H. Alaibadi and C.A. Brebbia, 1-46, Boston: Computational Mechanics Publications and Elsevier Applied Science.

[47] Kanninen, M.F. and C.H. Popelar. 1985. *Advanced Fracture Mechanics*. New York: Oxford University Press.

[48] Rooke, D.P. and D.J. Cartwright. 1976. *Compendium of Stress Intensity Factors*. Uxbridge: The Hillingdon Press.

[49] Murakami, Y. 1987. *Stress Intensity Factor Handbook, Volumes 1 and 2*. New York: Pergamon Press.

[50] Willis, J.R. 1972. The Penny-Shaped Crack on an Interface. Quart. J. Mech. and Appl. Math, 25[3]:367-385.

[51] Brebbia, C.A. and J. Dominguez. 1989. *Boundary Elements: An Introductory Course*. Boston: Computational Mechanics Publications and McGraw-Hill Book Company.

[52] Gomez-Lera, M.S. and E. Alarcon. 1987. Elastostatics. In *Boundary Element Methods in Mechanics,* Vol. 3, Computational Methods in Mechanics Series, ed. D.E. Beskos, 107-190, New York: North-Holland.

[53] Man, K.W., M.H. Aliabadi, and D.P. Rooke. 1993. Analysis of Contact Friction Using the Boundary Element Method. In *Computational Methods in Contact Mechanics*, eds. M.H. Aliabadi and C.A. Brebbia, 1-60, Boston: Computational Mechanics Publications and Elsevier Applied Science.

[54] Guiggiani, M. and A. Gigante. 1990. A General Algorithm for Multidimensional Cauchy Principal Value Integrals in the Boundary Element Method. *J. Appl. Mechs.*, 57: 906-915.

[55] Bialecki, R., R. Dallner, and G. Kuhn. 1993. New Application of Hypersingular Equations in the Boundary Element Method. *Comp. Methods. in Appl. Mechs. and Engin.*, 103: 399-416.

[56] Cruse, T.A. 1969. Numerical Solutions in Three Dimensional Elastostatics. *Int. J. Solids Structures*, 5: 1259-1274.

[57] Cruse, T.A. 1974. An Improved Boundary-Integral Equation Method for Three-Dimensional Elastic Stress Analysis. *Computers & Structures*, 4: 741-754.

[58] Pina, H.L.G., J.L.M. Fernandes, and C.A. Brebbia. 1981. Some Numerical Integration Formulae over Triangles and Squares with a 1/R Singularity. *Appl. Math. Modeling*, 5: 209-211.

[59] Lachat, J.C. and J.O. Watson. 1976. Effective Numerical Treatment of Boundary Integral Equations: A Formulation for Three-Dimensional Elastostatics. *Int. J. for Num. Methods in Engin.*, 10: 991-1005.

[60] Press, W.H. et. al. 1989. *Numerical Recipes: The Art of Scientific Computing*. New York: Cambridge University Press.

[61] Osterby, O. and Z. Zlatev. 1983. *Direct Methods for Sparse Matrices*. Lecture Notes in Computer Science Series. New York: Springer-Verlag.

[62] Dyck, V.A., J.D. Lawson, and J.A. Smith. 1984. *Fortran 77: An Introduction to Structured Problem Solving*. Reston: Reston Publishing Company, Inc.

Appendix A
Fundamental SIBEH Relations

Appendix A is included as a supplement to Chapters 2 and 3 which describe the surface integral and boundary element hybrid (SIBEH) method. This section, in conjunction with Appendix B, summarizes the fundamental relations of the technique and describes its development in detail sufficient for rederivation. The equations presented include the fundamental solutions, element mapping functions and element shape functions for both methods.

A.1 Fundamental Solutions - Surface Integral Method

The fundamental solutions on which the surface integral method is based can be derived from point-force elasticity solutions for three-dimensions and are analogous to the dislocation loop solutions useful in two-dimensional fracture mechanics. As described in Chapter 2, a combination of force dipoles (or multipole) is used to represent infinitesimal tensile and shear fracture events.

These influence functions have been developed from Kelvin's solution for a concentrated point-force acting in an infinite isotropic domain and from Rongved's solutions for a point force acting in one of two bonded semi-infinite regions [43]. These relations express the stress and displacements in media surrounding a point force in terms of Papkovitch-Neuber potential functions, **B** and β.

$$\sigma = \frac{2\nu\mu}{(1-2\nu)}(\nabla \cdot \mathbf{u})\mathbf{I} + \mu(\nabla \mathbf{u} + \mathbf{u}\nabla) \tag{A.1}$$

$$\mathbf{u} = \mathbf{B} - \frac{\nabla(\mathbf{r} \cdot \mathbf{B} + \beta)}{4(1-\nu)} \tag{A.2}$$

$$\text{with } \mu\nabla^2\mathbf{B} = 0 \text{ and} \mu\nabla^2\beta = 0$$

where σ and $\mathbf{u}$ represent the stresses and displacements at some point in the material described by position vector $\mathbf{r}$, μ and ν are material parameters, and B_X,B_Y, B_Z, and β are potential functions which depend upon the mechanical material properties and the locations of the sampling point and the force application point.

A.1.1 Kelvin's Point-Force Solution

For the simplest case of a concentrated point-force, $\mathbf{P}$, acting in an infinite homogeneous medium, the potential functions are:

$$B_i = \frac{P_i}{4\pi\mu\|\mathbf{r}\|} \ , \ \beta = 0 \tag{A.3}$$

A.1.2 Rongved's Point-Force Solution

For the more complicated case of a concentrated point-force acting in one of two bonded semi-infinite domains (Figure A.1), several sets of potential functions are required to completely describe the stress and displacement fields in both materials [43]. For a concentrated force acting perpendicular to the bimaterial interface:

$$B_x = B_y = 0 \quad \text{and} \quad B'_x = B'_y = 0 \tag{A.4a}$$

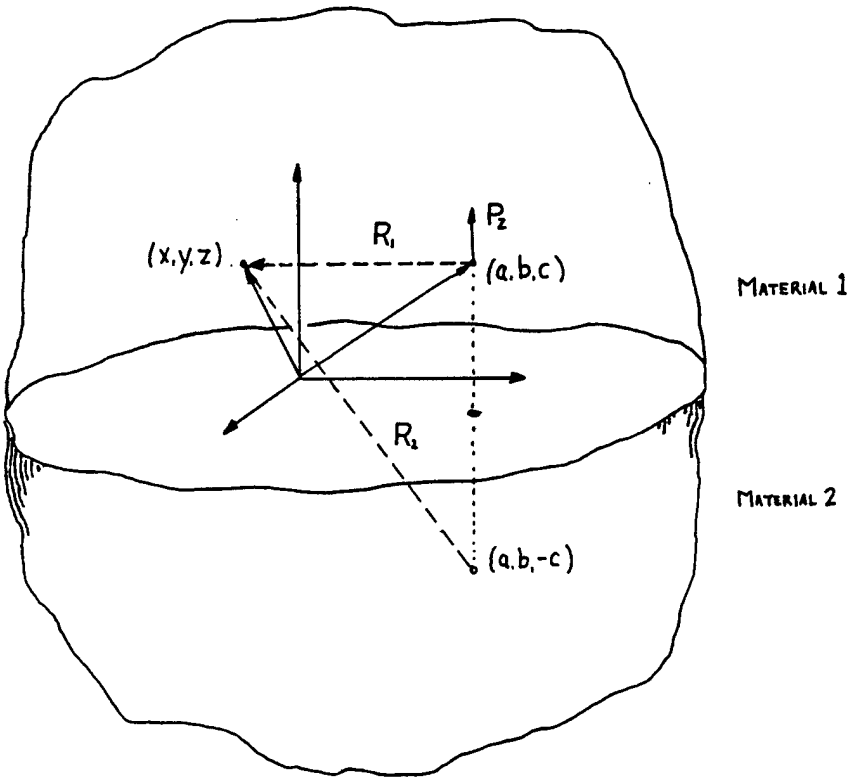

Figure A.1 Concentrated Force Acting in Bimaterial Domain; This figure depicts the reference coordinate frame used in Rongved's elasticity solution for a concentrated point-force acting in one of two semi-infinite, bonded materials.

$$B_z = \frac{P_z}{4\pi\mu}\left\{\frac{1}{R_1} + \frac{\mu-\mu'}{\mu+(3-4\nu)\mu'}\left[\frac{3-4\nu}{R_2} + \frac{2c(z+c)}{R_2^3}\right]\right\}$$

$$B'_z = \frac{(1-\nu')P_z}{\pi[\mu'+(3-4\nu')\mu]}\frac{1}{R_1} \qquad \text{(A.4b)}$$

$$\beta = \frac{-P_z}{4\pi\mu}\left\{\frac{c}{R_1} + \frac{\mu-\mu'}{\mu+(3-4\nu)\mu'}\left[\frac{c(3-4\nu)}{R_2}\right.\right.$$

$$\left.\left. - \frac{4(1-\nu)\mu\left[(1-2\nu)(3-4\nu') - 2\frac{\nu-\nu'}{\mu-\mu'}\mu'\right]}{\mu'+(3-4\nu')\mu}\log(R_2+z+c)\right]\right\}$$

$$\beta' = P_z \frac{(1-\nu')}{(1-\nu)}\left[-g_1 \frac{1}{R_1} + g_2 \log(R_2 - z + c)\right] \tag{A.4c}$$

with $$g_1 = \frac{(1-\nu)c}{\pi[\mu + (3-4\nu)\mu']},$$

$$g_2 = \frac{(1-\nu)[\mu(1-2\nu)(3-4\nu') - \mu'(1-2\nu')(3-4\nu)]}{\pi[\mu + (3-4\nu)\mu'][\mu' + (3-4\nu')\mu]},$$

$$R_1 = \left[(x-a)^2 + (y-b)^2 + (z-c)^2\right],$$

and $$R_2 = \left[(x-a)^2 + (y-b)^2 + (z+c)^2\right] \tag{A.4d}$$

where the unprimed and primed terms pertain to the two distinct material regions $z \geq 0$ and $z \leq 0$ respectively and the parameters (x,y,z) and (a,b,c) are the sampling and force-application point coordinates.

Similar potential functions have been derived for a force acting parallel to the interface and are included here for a the case of a concentrated force acting in the direction of the x-axis:

$$B_x = \frac{P_x}{4\pi\mu}\left\{\frac{1}{R_1} + \frac{\mu - \mu'}{\mu + \mu'}\frac{1}{R_2}\right\}$$

$$B'_x = \frac{P_x}{2\pi(\mu + \mu')}\frac{1}{R_1} \tag{A.5a}$$

$$B_y = B'_y = 0 \tag{A.5b}$$

$$B_z = \frac{(\mu - \mu')P_x}{2\pi[\mu + (3-4\nu)\mu']}\left\{\frac{-c(x-a)}{\mu R_2^3} + \frac{1-2\nu}{\mu + \mu'}\frac{(x-a)}{R_2(R_2 + z + c)}\right\}$$

$$B'_z = \frac{(1-2\nu')(\mu-\mu')P_x}{2\pi(\mu+\mu')[\mu'+(3-4\nu')\mu]} \frac{(x-a)}{R_1(R_1-z+c)} \qquad \text{(A.5c)}$$

$$\beta = \frac{P_x}{2\pi(\mu+\mu')[\mu+(3-4\nu)\mu']} \left\{ \frac{(1-2\nu)(\mu-\mu')c(x-a)}{R_2(R_2+z+c)} + h_1 \frac{(x-a)}{R_2+z+c} \right\}$$

$$\beta' = \frac{(1-\nu')P_x}{2\pi(1-\nu)(\mu+\mu')[\mu+(3-4\nu)\mu']} \left\{ [(1-2\nu)(\mu-\mu')+h_2]\frac{c}{R_1} + [h_1+h_2] \right\} \frac{(x-a)}{(R_1-z+c)} \qquad \text{(A.5d)}$$

$$\text{with } h_1 = \frac{1}{[\mu'+(3-4\nu')\mu]} \{ [(3-4\nu)(1-2\nu')\mu' - (3-4\nu')(1-2\nu)\mu] (\mu-\mu')(1-2\nu) - 2\mu'(\nu-\nu')[\mu'+(3-4\nu')\mu] \}$$

$$\text{and } h_2 = \frac{(\nu-\nu')[\mu+(3-4\nu)\mu']}{1-\nu'} \qquad \text{(A.5e)}$$

A.1.3 Displacement Discontinuity Solutions

From these potential representations, stress and displacement solutions can be derived for the force dipoles which comprise the displacement discontinuity model. These dipole solutions are derived using a limiting process for two parallel, opposing forces, **P**, separated by an infinitesimal distance, **h**. Taking the limit of the stress and displacement fields surrounding this force couple as $\mathbf{h} \rightarrow 0$ (with the dipole magnitude, **Ph**, held constant) gives the dipole solutions in terms of derivatives of the potential functions taken with respect to the distinguishing distance, **h** [35]. Equations (A.6) and

(A.7) represent the stress and displacement solutions for a dipole composed of forces in the κ direction combined using a limiting process in the λ direction.

$$\sigma_{ij,\lambda}^{(\kappa)} = \frac{\mu}{2(1-\nu)}\Big\{2\nu\delta_{ij}B_{k,k\lambda}^{(\kappa)} + (1-2\nu)\Big(B_{i,j\lambda}^{(\kappa)} + B_{j,i\lambda}^{(\kappa)}\Big) - r_m B_{m,ij\lambda}^{(\kappa)} + B_{\lambda,ij}^{(\kappa)} - \beta_{,ij\lambda}^{(\kappa)}\Big\} \tag{A.6}$$

$$u_{i,\lambda}^{(\kappa)} = \frac{1}{4(1-\nu)}\Big\{(3-4\nu)B_{i,\lambda}^{(\kappa)} - r_m B_{m,i\lambda}^{(\kappa)} + B_{\lambda,i}^{(\kappa)} - \beta_{,i\lambda}^{(\kappa)}\Big\} \tag{A.7}$$

where $i,j,k,m \in \{x,y,z\}$ and $\kappa,\lambda \in \{a,b,c\}$

Equations (A.6) and (A.7) are expressed in indicial notation so that a comma in the subscript denotes differentiation with respect to the trailing variables and repeated indices signify summation. These dipole relations are combined to form multipoles (as described in Chapter 2 and depicted in Figure 2.1) and are then converted to displacement discontinuity solutions with a combination of material parameters [35]. For a tensile multipole aligned with the z-axis:

$$\sigma_{ij} = -\delta_{COD}\left[\frac{2\mu(1-\nu)}{(1-2\nu)}\right]\left\{\sigma_{ij,c}^{(z)} + \frac{\nu}{(1-\nu)}\Big(\sigma_{ij,a}^{(x)} + \sigma_{ij,b}^{(y)}\Big)\right\} \tag{A.8}$$

$$u_i = -\delta_{COD}\left[\frac{2\mu(1-\nu)}{(1-2\nu)}\right]\left\{u_{i,c}^{(z)} + \frac{\nu}{(1-\nu)}\Big(u_{i,a}^{(x)} + u_{i,b}^{(y)}\Big)\right\} \tag{A.9}$$

For a shear dipole acting in the x-z directions:

$$\sigma_{ij} = -\delta_{SHEAR}[\mu]\left\{\sigma_{ij,c}^{(x)} + \sigma_{ij,a}^{(z)}\right\} \tag{A.10}$$

$$u_i = -\delta_{SHEAR}[\mu]\left\{u_{i,c}^{(x)} + u_{i,a}^{(z)}\right\} \tag{A.11}$$

A similar derivation process may be followed for fractures on or near planar bimaterial interfaces using Rongved's solutions (Section A.1.2). Once the bimaterial displacement discontinuity solutions have been formed, interfacial crack solutions can be generated by taking the limit as the infinitesimal fracture event approaches the interface from either material. (The two distinct solutions produce the same stress and displacement fields at this point.) Although somewhat more complicated, these functions can be treated with the same integration and solution schemes outlined for fractures in homogeneous media.

Because of the complexity involved in these derivations, the symbolic manipulator MACSYMA has been used for accurate derivation of the fundamental solutions. However, their uniqueness precludes straightforward verification. For this analysis, verification involved derivation and comparison of two distinct influence function sets, checks of symmetric properties, and comparison with related, previously derived fundamental solutions [35].

A.2 Fundamental Solutions - Boundary Element Method

The primary boundary element influence functions for three-dimensional elastostatics are also derived from Kelvin's elasticity solution for a concentrated force acting in an infinite isotropic domain [51]. Since complete derivations are presented in many reference texts, only the final function forms are included here. For the stress and displacement fields surrounding a unit point-force in the j-direction:

$$u_{ij}^{*} = \frac{1}{16\pi\mu(1-\nu)r}\left[(3-4\nu)\delta_{ij} + r_{,i}r_{,j}\right] \tag{A.12}$$

$$p^*_{ij} = \frac{1}{8\pi(1-\nu)r^2}\{\frac{\partial r}{\partial n}\left[(1-2\nu)\delta_{ij} + 3r_{,i}r_{,j}\right]$$

$$+(1-2\nu)\left(n_i r_{,j} - n_j r_{,i}\right)\} \qquad \text{(A.13)}$$

where u^*_{ij} represents the displacement components u_j at point **r** on the boundary element surface induced by a concentrated unit force, P_i, applied at the origin. p^*_{ij} represents the corresponding tractions at this surface with a local outward normal **n**.

For the boundary collocation formulation, Equations (A.12) and (A.13) are used to relate the boundary tractions and displacements. As outlined in Chapters 2 and 3, this common solution scheme results in a linear equation system which can be solved to obtain the boundary parameters. Once these boundary values have been calculated, the derivative influence functions $\mathbf{d}^*$ and $\mathbf{s}^*$ can be used to determine the stresses in the domain interior [51]. These derivative functions give the stresses acting at an internal point (e.g. crack surface) as a function of the boundary displacement and traction distributions respectively and are derived by differentiation of the fundamental solutions $\mathbf{u}^*$ and $\mathbf{p}^*$.

$$n_k d^*_{ijk} = \frac{1}{8\pi(1-\nu)r^2} n_k \left\{(1-2\nu)\left[\delta_{ij}r_{,k} + \delta_{ik}r_{,j} - \delta_{jk}r_{,i}\right]\right.$$

$$\left.+3r_{,i}r_{,j}r_{,k}\right\} \qquad \text{(A.14)}$$

$$n_k s^*_{ijk} = \frac{\mu}{4\pi(1-\nu)r^3} n_k \left\{3\frac{\partial r}{\partial n}\left[(1-2\nu)\delta_{jk}r_{,i} + \nu\left(\delta_{ij}r_{,k} + \delta_{ik}r_{,j}\right)\right.\right.$$

$$\left.-5r_{,i}r_{,j}r_{,k}\right] + 3\nu\left(n_j r_{,i}r_{,k} + n_k r_{,i}r_{,j}\right)$$

$$\left.+(1-2\nu)\left[3n_i r_{,j}r_{,k} + n_j\delta_{ik} + n_k\delta_{ij}\right] - (1-4\nu)n_i\delta_{jk}\right\} \qquad \text{(A.15)}$$

Note that for these derivative relations the radial vector, **r**, extends from the internal point towards the external boundary and that all derivatives of this vector are taken at the boundary point.

A.3 Element Mapping Functions

The element mapping functions incorporated in the matrix crack analysis code are based on the bi-quadratic Lagrange functions and relate the local element reference frame to the global coordinate frame [45]:

$$\mathbf{x}(\xi) = \sum \mathrm{M}^{(\alpha)}(\xi)\mathbf{x}^{\alpha} \quad \alpha = 1,2,3,...,9 \tag{A.16}$$

where $\mathrm{M}^{(1)}(\xi_1,\xi_2) = \frac{1}{4}\xi_1\xi_2(\xi_1-1)(\xi_2-1)$ (A.17a)

$$\mathrm{M}^{(2)}(\xi_1,\xi_2) = \frac{1}{4}\xi_1\xi_2(\xi_1+1)(\xi_2-1) \tag{A.17b}$$

$$\mathrm{M}^{(3)}(\xi_1,\xi_2) = \frac{1}{4}\xi_1\xi_2(\xi_1+1)(\xi_2+1) \tag{A.17c}$$

$$\mathrm{M}^{(4)}(\xi_1,\xi_2) = \frac{1}{4}\xi_1\xi_2(\xi_1-1)(\xi_2+1) \tag{A.17d}$$

$$\mathrm{M}^{(5)}(\xi_1,\xi_2) = \frac{1}{2}\xi_2(\xi_1^{\,2}-1)(\xi_2+1) \tag{A.17e}$$

$$\mathrm{M}^{(6)}(\xi_1,\xi_2) = \frac{1}{2}\xi_1(\xi_1+1)(\xi_2^{\,2}-1) \tag{A.17f}$$

$$\mathrm{M}^{(7)}(\xi_1,\xi_2) = \frac{1}{2}\xi_2(\xi_1^{\,2}-1)(\xi_2-1) \tag{A.17g}$$

$$\mathrm{M}^{(8)}(\xi_1,\xi_2) = \frac{1}{2}\xi_1(\xi_1-1)(\xi_2^{\,2}-1) \tag{A.17h}$$

$$\mathrm{M}^{(9)}(\xi_1,\xi_2) = (\xi_1^{\,2}-1)(\xi_2^{\,2}-1) \tag{A.17i}$$

Simpler mapping functions are included in this set by condensation. For example, linear boundaries are approximated by parabolically curved boundary segments for which the midpoint is located directly between the neighboring corner nodal points. Similarly, triangular elements are included by condensing the third and fourth nodal points and by combining the related mapping functions.

A.4 Element Shape Functions

A variety of local distribution functions have been included for approximating tractions and displacements along fracture surfaces and component boundaries. Three shape functions have been implemented for the surface integral model - constant, constant-linear, and crack-tip elements [26]. The corresponding shape functions are outlined below:

$$\delta(\xi) = \delta^1 \tag{A.18}$$

$$\delta(\xi) = \tfrac{1}{2}(\delta^1 + \delta^2) + (\delta^2 - \delta^1)\xi_2 \tag{A.19}$$

$$\delta(\xi) = \mathrm{N}_1(\rho(\xi))\delta^1 + \mathrm{N}_1(\rho(\xi))\delta^2 \tag{A.20}$$

$$\text{with } \rho(\xi) = \left\| \mathbf{x}(\xi_1, \xi_2) - \mathbf{x}(\xi_1, 0) \right\| \tag{A.21}$$

where δ^1 and δ^2 are the crack opening displacements at the collocation points and $N_1(\xi)$ and $N_2(\xi)$ are orthogonal functions of the actual crack-tip radius, ρ. These functions are based on the first two terms of the Williams expansion for fractures in homogeneous media and are presented in complete form in Equation 2.12.

For the isoparametric boundary element formulation, the shape functions will be equivalent to the mapping functions given in section A.3 above.

$$N^{\alpha}(\xi) = M^{\alpha}(\xi) \text{ for } \alpha = 1..9 \tag{A.22}$$

The Lagrange family of functions is preferred in this case because it results in more uniform collocation point distributions and therefore greater solution accuracy. Lower order variations and other function families (e.g. serendipity) can be simulated as linear combinations of the nine-noded Lagrange functions presented above.

Appendix B

Singular Integration Schemes

Appendix B has been included as a supplement to Chapters 2 and 3 to provide a more detailed development of the singular integration schemes used in the SIBEH method. Singular integral regularization procedures are outlined for both the surface integral and boundary element methods. These approaches are useful both for evaluation of genuinely singular integrals and for reduction of computational errors in nearly-singular integrals.

B.1 Singular Integration - Surface Integral Method

Singular integration of the fundamental stress and displacement solutions for the surface integral model use similar approaches (i.e. regularization by subtraction of a rigid body motion) but are handled in slightly different manners due to a difference in the dominant singularity order.

As presented in Section 2.2, the singular integral for stresses can be reduced to a tractable form by subtracting a rigid body motion (i.e. constant displacement over the entire fracture plane, S_T) which contributes nothing to the stress fields.

$$C_{IJ} = n\int_{S_e^{(J)}} \gamma^s N^{(J)}(\zeta) dA \tag{B.1}$$

$$C_{IJ} = n\int_{S_e^{(J)}} \gamma^s (N^{(J)}(\zeta) - N_0^{(J)}) dA + N_0^{(J)} n\int_{S_e^{(J)}} \gamma^s dA \tag{B.2}$$

$$= n\int_{S_e^{(J)}} \gamma^s (N^{(J)}(\zeta) - N_0^{(J)}) dA - N_0^{(J)} n \int_{S_T - S_e^{(J)}} \gamma^s dA \tag{B.3}$$

$$\text{using} \quad N_0^{(J)} n \int_{S_T} \gamma^s dA = 0 \tag{B.4}$$

where the original integral of γ^s (the fundamental stress solution) is evaluated over $S_e^{(J)}$ (the elemental regions surrounding collocation point J), $N^{(J)}$ combines the element shape functions associated with this point J, $N_o^{(J)}$ is the shape function value at J, and **n** denotes the normal direction associated with the sampling point.

The first integral in Equation (B.3) is now defined in a Cauchy principal value sense and can be evaluated numerically. When the quadrature point coordinates are taken to be symmetric about the singular point, Gauss-Legendre quadrature orders as low as 2 can be used to obtain accurate integral solutions.

The remaining term in Equation (B.3) involves integration of the fundamental stress solution over the region $S_T - S_e^{(J)}$ (i.e. the entire fracture plane excepting the elemental regions surrounding point J). Though impractical to evaluate with two-dimensional quadrature, this integral is defined because of the $1/R^3$ influence function singularity and because of the exception of point J from the integration region. Further simplification is attained by conversion to a local polar coordinate reference frame, which reduces the dominant singularity by one order and facilitates analytical integration of the radial terms.

$$\int_{S_T - S_e^{(J)}} \gamma^s dA = \iint_{S_T - S_e^{(J)}} \left[\sum \gamma_\theta^s(\theta) \gamma_R^s(r,z)\right] r dr \, d\theta \tag{B.5}$$

$$= \sum \int \gamma_\theta^s(\theta) \int_{r(\theta)}^{\infty} \gamma_R^s(r,z) r dr \, d\theta \tag{B.6}$$

$$= -\sum \int \gamma_\theta^s(\theta) \Gamma_R^s(\theta,z) d\theta \tag{B.7}$$

$$\text{where} \quad \Gamma_R^s(\theta,z) = \int_{r(\theta)}^{\infty} \gamma_R^s(r,z) r dr \tag{B.8}$$

In this case, the radial integral expressed in Equation (B.8) is evaluated from the element boundary, $r(\theta)$, to infinity, where the 1/R singularity of $\Gamma^s_R(r,z)$ reduces the contribution at this bound to zero. To simplify the one-dimensional integration in Equation (B.7) for parabolically curved boundaries, each element boundary segment is represented parametrically.

$$\int_{S_T - S_e^{(J)}} \gamma^s dA = \sum \int_{-1}^{1} \gamma^s_\theta(\theta(\varsigma)) \Gamma^s_R(\theta(\varsigma), z) \frac{d\theta}{d\varsigma} d\varsigma \tag{B.9}$$

Evaluation of the fundamental displacement solution for proximal points follows a similar approach, though the evaluation of the regularizing integral is handled differently because of the lower order of the dominant singularity ($1/R^2$). Subtraction of a rigid body motion over the entire fracture plane is not required. As in the stress solution case, a constant regularizing term, $N_0^{(J)}$, is removed to define the Cauchy principal value integral.

$$n\int_{S_e^{(J)}} \gamma^d N^{(J)}(\zeta) dA = n\int_{S_e^{(J)}} \gamma^d (N^{(J)}(\zeta) - N_0^{(J)}) dA$$

$$+ N_0^{(J)} n \int_{S_e^{(J)}} \gamma^d dA \tag{B.10}$$

In this case, though, the regularizing integral is evaluated in a semi-analytic fashion over $S_e^{(J)}$, the elemental region surrounding collocation point J.

$$\int_{S_e^{(J)}} \gamma^d dA = \sum \int \gamma^d_\theta(\theta) \int_0^{r(\theta)} \gamma^d_R(r,z) r dr \, d\theta \tag{B.11}$$

$$= \sum \int \gamma^d_\theta(\theta) \Gamma^d_R(\theta, z) d\theta \tag{B.12}$$

$$\text{where } \Gamma^d_R(\theta, z) = \lim_{\varepsilon \to 0} \int_\varepsilon^{r(\theta)} \gamma^d_R(r,z) r dr \tag{B.13}$$

Existence of this integral term requires that the angular integral for a circular contour (constant radius) be finite.

$$\lim_{\varepsilon \to 0} \Gamma_R^d(\varepsilon, z) \left[\sum \int \gamma_\theta^d(\theta) d\theta \right] = 0 \tag{B.14}$$

This property is satisfied by the fundamental displacement solutions for cases of interest in the surface integral and boundary element hybrid approach.

B.2 Singular Integration - Boundary Element Method

Two cases of singular integration occur regularly in boundary element analysis. These involve evaluation of the primary fundamental solutions, **u*** and **p***, over an elemental region coincident with the collocation point at which tractions and displacements are evaluated. Other singular situations are possible in the hybrid formulation (e.g. a surface integral collocation point coincident with the boundary element surface) but occur only in improperly posed problems. This section outlines an integration scheme developed recently for general boundary element applications [44,57].

The implemented technique eliminates the singularity of the integral by subtracting a Taylor series expansion of the integrand about the singular point. For little additional cost compared with more traditional integration procedures, the technique also provides more accurate results for proximal sampling points. Although the two methods were developed independently, the singular integration method presented above for fracture solutions can be viewed as a specialized form of this approach. A formal derivation and demonstration has been presented but is outlined here for completeness [44]. Because the fundamental solution singularities are one order lower ($1/R^2$ and $1/R$ respectively for stresses and displacements) than those for fracture events, the restriction to planar elements and internal collocation points can be relaxed.

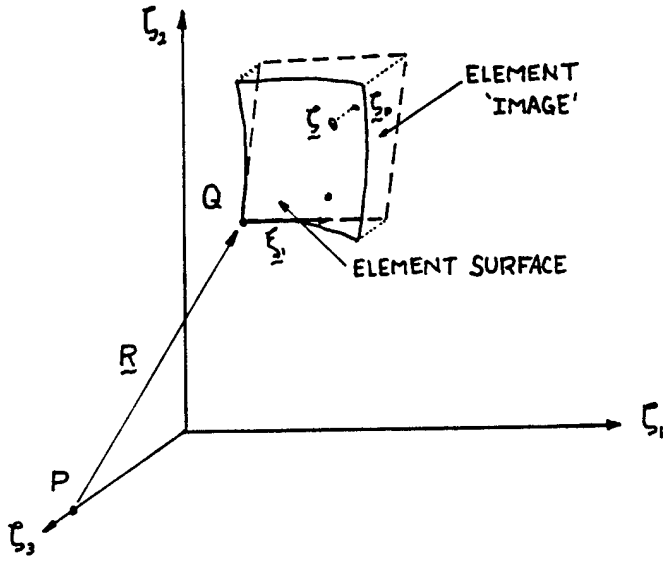

Figure B.1 Local Coordinate Frame used for Singular Integration Scheme Local co-ordinates, ζ, are defined such that the ζ_1-ζ_2 plane is tangent to the element surface at the nearest collocation point and the origin is the projection of the sampling point into this plane. The regularizing integral terms are evaluated and integrated in this tangent plane. (Adapted from Reference [44])

To simplify the regularization procedure for the general case of curved boundary elements, the integral is evaluated in a coordinate frame defined by a plane (ζ_1-ζ_2 plane) tangent to the element at the collocation point, Q, nearest to the source point, P. Further, the coordinate frame is defined such that the ζ_1-direction and element-defined ξ_1-direction are parallel and the origin is located at the projection of the source point onto this plane (See Figure B.1). This conversion facilitates the development and integration of the regularizing terms in the local tangent plane.

Projections of points on the element surface, or 'image' points, can be expressed as a linear combination of mapping functions and the nodal point projections and are designated here with a prime:

$$\zeta'_I(\xi) = \sum M^{\alpha}(\xi)\zeta_I^{\alpha}, \quad \alpha = 1,\ldots,9, I = 1,2 \tag{B.16}$$

The regularizing terms used to reduce the integral singularity consist of the fundamental solution, a first-order Taylor series expansion of the displacements or tractions (L_Q), and the differential area dA' all evaluated at the image points in the tangent plane.

$$\int_{S_e^{(j)}} f^*(\zeta_P,\zeta)N(\zeta)dA = \int_{S_e^{(j)}} \left\{ f^*(\zeta_P,\zeta)N(\zeta)dA - f^*(\zeta_P,\zeta')L_Q(\zeta')dA' \right\} + \int_{S_e^{(j)}} f^*(\zeta_P,\zeta')L_Q(\zeta')dA' \tag{B.17}$$

where $f^*(\zeta_o,\zeta)$ and $f^*(\zeta_o,\zeta^P)$ represent either of the fundamental solutions evaluated on the element surface and on the tangent plane (respectively) and,

$$L_Q(\zeta) = N(\zeta_o) + \left.\frac{\partial N}{\partial \zeta_1}\right|_Q (\zeta'_1 - \zeta_1^Q) + \left.\frac{\partial N}{\partial \zeta_2}\right|_Q (\zeta'_2 - \zeta_2^Q) \tag{B.18}$$

As a result of the coordinate transformation described earlier, the derivative terms in Equation (B.18) can be estimated at the point Q as a linear function of the mapping function derivatives and nodal point coordinates.

This expansion about Q can be shown to completely negate the singularity in the boundary element fundamental solutions, resulting in a non-singular boundary element formulation. In addition, evaluation of the regularizing terms within the tangent plane allows them to be expressed in an analytically integrable form. Using an approach

similar to that developed above for fracture solutions, the planar function forms are converted to a local cylindrical coordinate frame and separated into products of radial and angular terms. The radial terms are analytically integrated from the origin to the element boundary image. Finally, the combined angular terms can be integrated using low-order one-dimensional quadrature.

Although this integration scheme permits evaluation of stress and displacement fields nearer to the element surface than previously possible, it is not generally the most cost-effective approach. For source points further from the element than the element dimension, straightforward two-dimensional numerical integration gives equivalent results at less expensive.